INTERNATIONAL JOURNAL FOR NUMERICAL METHODS IN FLUIDS
Int. J. Numer. Meth. Fluids **28**: 571–600 (1998)

THE INTERACTION OF BACKGROUND OCEAN AIR BUBBLES WITH A SURFACE SHIP

P.M. CARRICA, F.J. BONETTO, D.A. DREW* AND R.T. LAHEY, JR.
Center for Multiphase Research, Rensselaer Polytechnic Institute, Troy, NY 12180-3590, USA

SUMMARY

A two-fluid model suitable for the calculation of the two-phase flow field around a naval surface ship is presented. This model couples the Reynolds-averaged Navier–Stokes (RANS) equations with equations for the evolution of the gas-phase momentum, volume fraction and bubble number density, thereby allowing the multidimensional calculation of the two-phase flow for monodisperse variable size bubbles. The bubble field modifies the liquid solution through changes in the liquid mass and momentum conservation equations. The model is applied to the case of the scavenging of wind-induced sea-background bubbles by an unpropelled US Navy frigate under non-zero Froude number boundary conditions at the free surface. This is an important test case, because it can be simulated experimentally with a model-scale ship in a towing tank. A significant modification of the background bubble field is predicted in the wake of the ship, where bubble depletion occurs along with a reduction in the bubble size due to dissolution. This effect is due to lateral phase distribution phenomena and the generation of an upwelling plume in the near wake that brings smaller bubbles up to the surface. © 1998 John Wiley & Sons, Ltd.

KEY WORDS: two-phase flow; bubbly wake; ship hydrodynamics; multidimensional two-fluid model; spatial distribution of bubble size

1. INTRODUCTION

With the recent improvement of high-speed digital computers and the development of multidimensional models that allow calculation of two-phase flow [1], prediction of the distribution of bubbles in the wave field and in the wake of a surface ship has become feasible. The presence of bubbles can modify the total resistance, wave fields and propeller efficiency. Furthermore, the two-phase flow in the region close to the ship's hull will influence how the bubbly wake will look in the far field, where the presence of bubbles can be determined by measuring acoustic attenuation [2]. It is the interest in the two-phase flow in the region close to the ship, and its effect on the bubbly wake for signature estimations, that has motivated this work.

In the case of a ship, bubbles can be entrained by several mechanisms. Breaking bow and stern waves, spilling waves, boundary layer air entrainment and propeller cavitation and/or ventilation can cause air to be entrained into the ocean. All these mechanisms are caused by hull–surface interaction or by the propeller. In addition, bubbles are naturally present in the sea due to wind-induced breaking and spilling, wave–wave interactions, etc. These mechanisms are dependent on the sea and weather conditions, and the degree of air entrainment remains

---

* Correspondence to: Center for Multiphase Research, Rensselaer Polytechnic Institute, Troy, NY 12180-3590, USA.

CCC 0271–2091/98/140571–30$17.50

Received 5 July 1996
Revised 25 June 1997

unknown at the present and is subject of further research. A surface ship can create a bubbly wake by two means: by causing bubble entrainment or by scavenging the existing background bubbles in the sea. In both cases the ship may cause a significant modification of the ambient bubble field.

The interaction of bubbles with a surface ship involves several processes. Buoyancy contributes to the accumulation of bubbles below the hull of the ship and to loss of bubbles through the surface. In most of the cases, lift forces may also attract bubbles towards the hull. Other forces such as the virtual mass force and the lateral pressure gradients exhibit more complex behavior. In addition, the bubbles can dissolve (or grow), depending on the local pressure, the size of the bubble and dissolved air concentration in the water. To complete the picture, the liquid velocity and pressure fields are modified by the presence of bubbles through introduction of interfacial forces, changes in the continuity equation and in the resultant turbulent field.

To study these effects, simulations were performed using the geometry of a typical naval combatant, the US Navy frigate FF-1052, shown in Figure 1. This ship offers a complex geometry with bulbous bow and transom stern, and has been studied numerically for the single phase case with and without a propeller, with non-zero Froude number boundary conditions at the free-surface and for the unpropelled ship in bubbly two-phase flow for the case of zero Froude number [3]. Some experimental data exist for the case of single-phase flow, for the model-scale FF-1052 [4–6], but unfortunately, no experimental results are available for any case of two-phase flow around the ship. The only available data related to the two-phase flow around a ship is the acoustic response in the far wake, several ship lengths behind the stern [2]. This lack of experimental results is not surprising, considering that model-scale ships do not entrain bubbles and data acquisition at full-scale is very complex and expensive. In this regard, the study of the two-phase flow field caused by a ship moving through the ocean having a background of bubbles is appealing because it is possible to perform controlled experiments with model-scale in towing tanks injecting a sheet of bubbles in front of the ship.

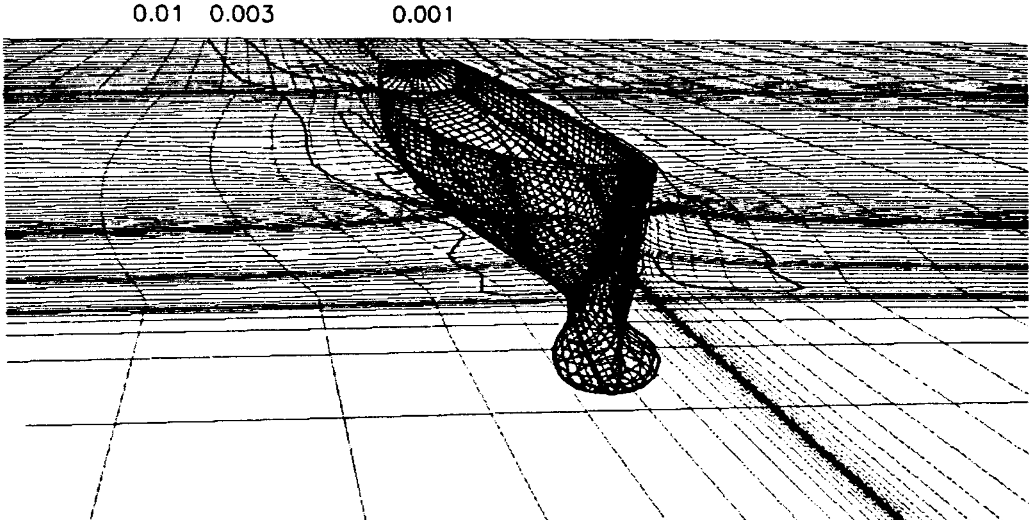

Figure 1. US Navy FF-1052 and free surface. The contour lines represent constant gas volume fraction.

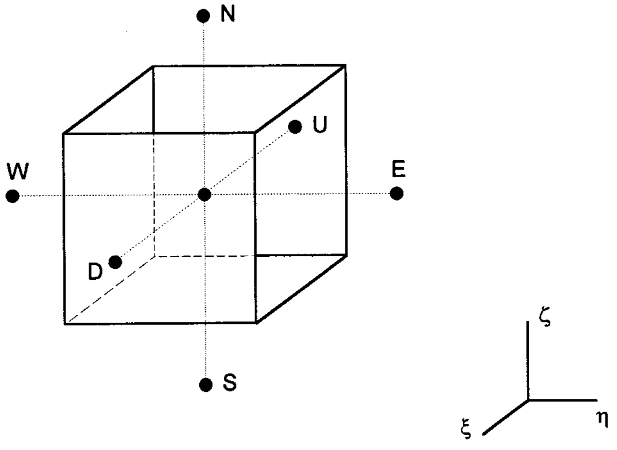

Figure 2. Control volume in the computational domain.

In this paper, a multidimensional model appropriate for calculating the two-phase flow around a naval surface ship is presented under free-surface boundary conditions, including several effects such as bubble dissolution and pressure effects, that cause the bubble radius to change as the bubbles are transported by the liquid. The model is applied to the case of the scavenging of background bubbles using free-sea data for the gas volume fraction and bubble number density boundary conditions.

At this stage of the study the main interest is in showing the feasibility of the calculations and the main trends observed in the two-phase flow, therefore some simplifications have been made in the numerical resolution of the liquid equations to make the calculations more economical. These include the use of a zero-order turbulence model and somewhat coarse grids. These simplifications are also justified by the present impossibility of validation of the numerical results due to the lack of experimental data in the subject.

2. MATHEMATICAL MODEL

The starting point for the modeling of the two-phase flow phenomena is a mechanistically based multidimensional two-fluid model. [1,7–10]. The following conditions are assumed:

1. The bubbles have negligible inertia ($\rho_g \ll \rho_l$). This assumption holds for air–water flows at the pressures expected in the flow near a high speed surface ship.
2. The bubbles are spherical. This hypothesis is reasonable since very small bubbles are present in the flows under consideration.
3. The liquid is incompressible.

The ensemble-averaged continuity and momentum equations for the gas and liquid phases in the two-fluid model can be written in Cartesian tensor notation as

$$\frac{\partial \alpha_k \rho_k}{\partial t} + \frac{\partial}{\partial x_j}(\alpha_k \rho_k u_{k,j}) = S_k, \tag{1}$$

$$\frac{\partial \alpha_k \rho_k u_{k,i}}{\partial t} + \frac{\partial}{\partial x_j}(\alpha_k \rho_k u_{k,i} u_{k,j}) = \frac{\partial}{\partial x_j}[\alpha_k(\tau_{k,ij} + \tau_{k,ij}^{Re})] + M_{k,i} + \alpha_k \rho_k g \delta_{i3}, \tag{2}$$

where $k = \mathrm{g}$ or l denotes the gas or liquid phase, α_k is the phasic volume fraction, ρ_k is the phasic density, $u_{k,i}$ is the velocity of phase-k, $\tau_{k,ij}$ and $\tau_{k,ij}^{Re}$ are the viscous stress tensor and the turbulent stress tensor of phase-k, $M_{k,i}$ is the interfacial momentum transfer between the phases, and the last term on the right-hand-side of Equation (2) is the gravitational force.

A mass source S_k is included in Equation (1). In this work, this source is exclusively due to the gas dissolution into the liquid, and can be positive or negative. Since this process is very slow, its effect in the momentum transfer between the phases is negligible. In addition, due to the relatively small gas volume fractions present in the flow and assumption 1, this mass source is negligible for the liquid phase.

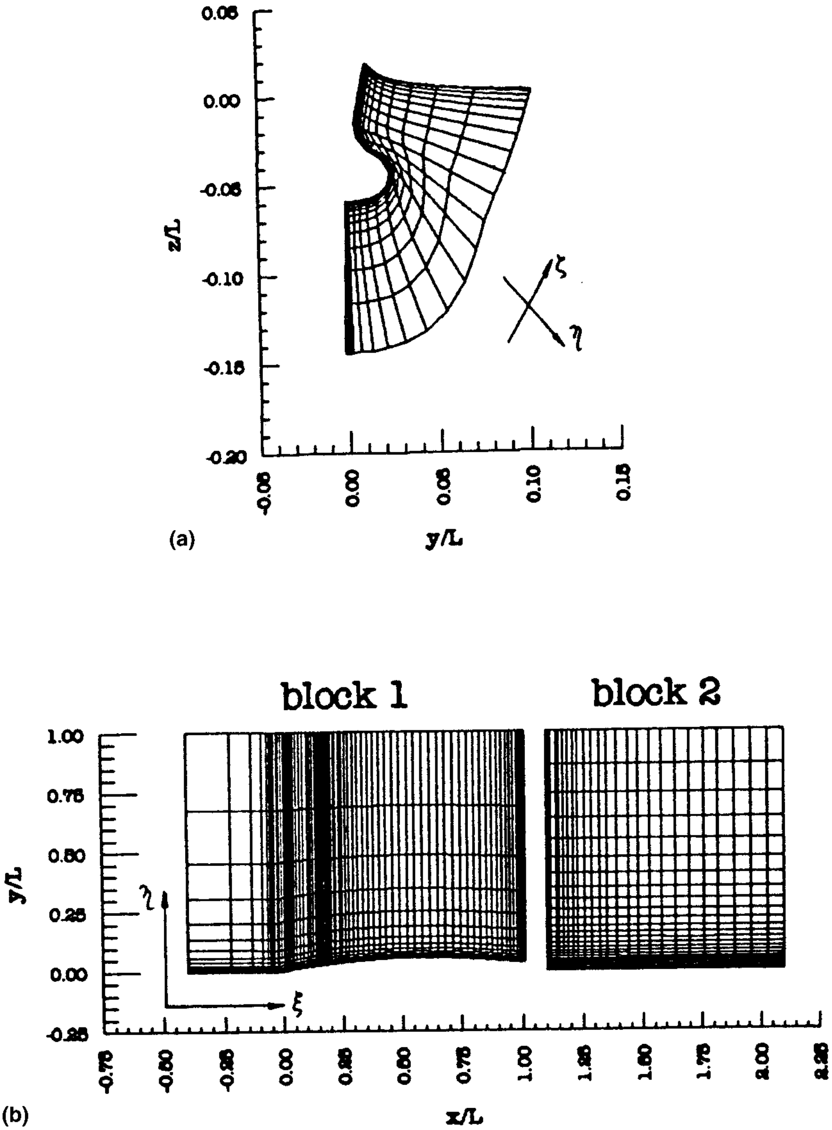

Figure 3. Multi-block grid. (a) Crossplane of block 1 at $x/L = 0.05$. Only the first 25 nodes in the η-direction are shown for clarity. (b) Longitudinal free-surface plane. The blocks are intentionally separated for clarity.

Table I. Integral quantities used to test grid convergence

	Value	x	y	z
$P_{\max}$	0.344, 0.395, 0.398, 0.408	0.023, 0.022, 0.0216, 0.0216	Hull	-0.044, -0.038, -0.042, -0.042
$P_{\min}$	-0.19, -0.23, -0.23, -0.23	0.056, 0.0445, 0.0445, 0.0445	Hull	-0.055, -0.0573, -0.0573, -0.0573
$\alpha_{\max}$ (%)	3.03, 3.8, 4.02, 4.1	0.081, 0.99, 1.0, 1.0	Hull	Free surface
$N_{\max}$ (%)	3.11, 11.6, 11.6, 11.8	0.081, 0.99, 1.0, 1.0	Hull	Free surface
$Z_{\max}$ ($\times 10^{-2}$)	2.14, 2.3, 2.29, 2.29	0.056, 0.056, 0.056, 0.056	Hull	Free surface
$Z_{\min}$ ($\times 10^{-3}$)	-5.45, -2.02, -2.04, -2.01	0.85, 0.50, 0.52, 0.555	Hull	Free surface
$\lvert\vec{u}_g\rvert_{\max}$	1.05, 1.074, 1.079, 1.077	0.397, 0.445, 0.445, 0.445	108, 105, 104, 103 ($\times 10^{-5}$)	-0.061, -0.063, -0.064, -0.065

The values in each cell are given for the very coarse, coarse, medium and fine grids.

For the sake of simplicity, α denotes the gas volume fraction, thus $\alpha = \alpha_g$ and $\alpha_l = 1 - \alpha$. Using assumption 3, the mass conservation equations (1), can be written in indicial form as

$$\frac{\partial(1-\alpha)}{\partial t} + \frac{\partial[(1-\alpha)u_{l,j}]}{\partial x_j} = 0, \tag{3}$$

$$\frac{\partial(\rho_g \alpha)}{\partial t} + \frac{\partial(\rho_g \alpha u_{g,j})}{\partial x_j} = S_g. \tag{4}$$

In contrast to the liquid density, the gas density ρ_g cannot be considered constant, due to the large pressures present at the bottom of the ship and near the bow. A simple model consisting of the ideal gas relation, coupled with hydrostatic pressure, is used to calculate the gas density at every point in the flow field

$$\rho_g = (\rho_l g z + p)\frac{\rho_{g,o}}{p_o}, \tag{5}$$

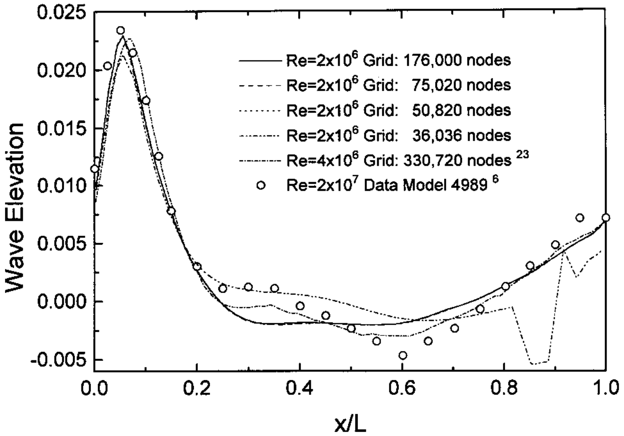

Figure 4. Wave profiles at the hull.

where z is the vertical distance to the free surface, and p_o and $\rho_{g,o}$ are the pressure and the density of the gas just over the surface (i.e. at atmospheric pressure).

The mass dissolution rate of a bubble is calculated from the expression given by Levich [11] and used by Hyman [2] to calculate the far-field bubbly wake of a ship

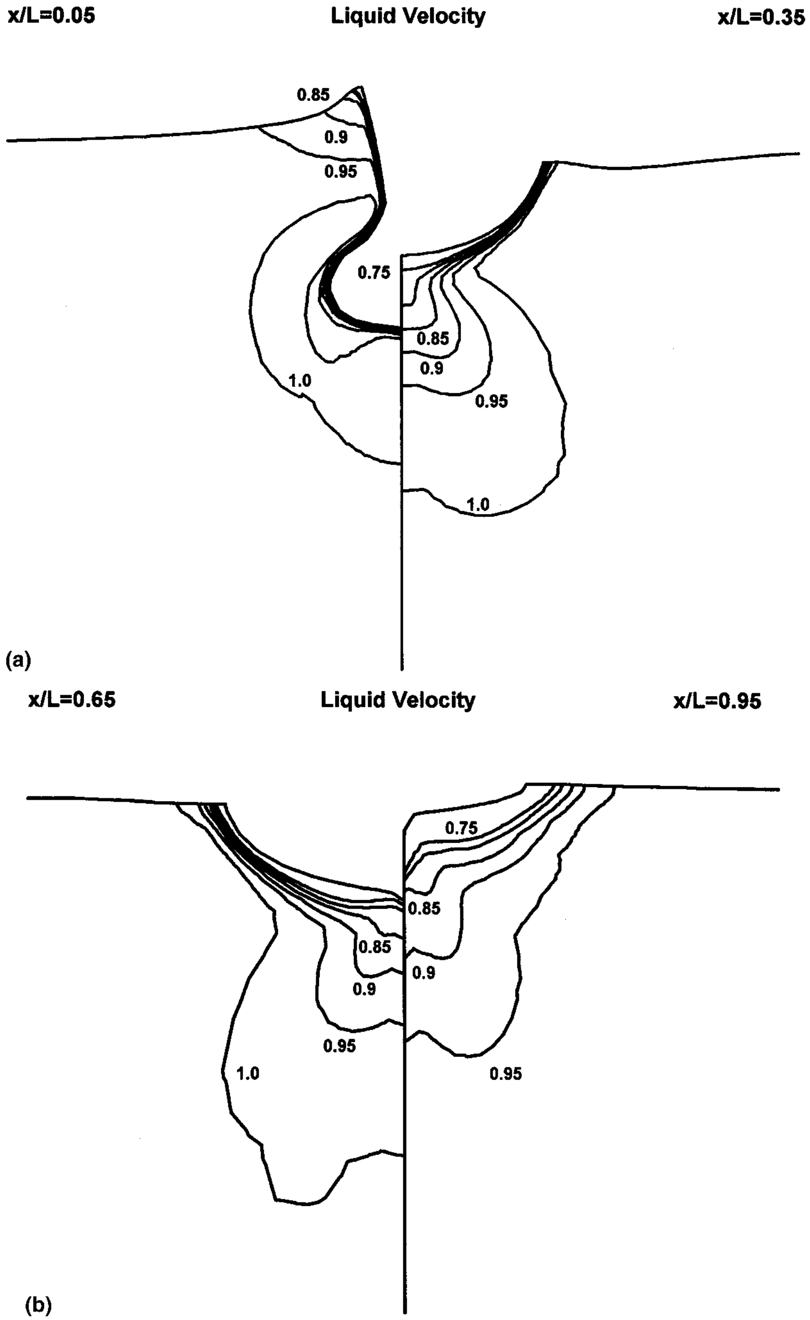

Figure 5. Liquid axial velocity for $x/L = 0.05$, 0.35, 0.65, 0.95, 1.05 and 1.35.

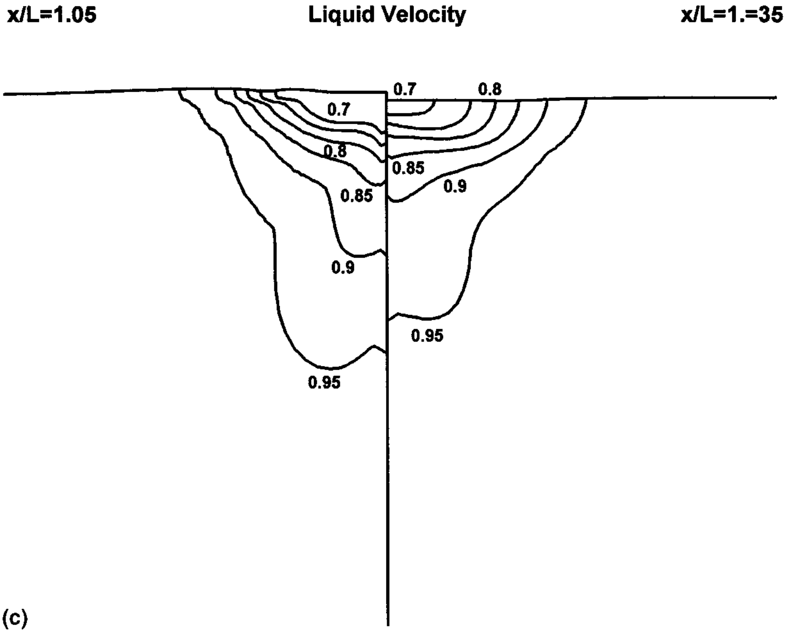

Figure 5 (*Continued*)

$$\frac{\mathrm{d}m}{\mathrm{d}t} = 8(C_\infty - C_0)\kappa^{2/3}|u_\mathrm{r}|^{1/3}r_\mathrm{b}^{4/3}, \tag{6}$$

where r_b is the bubble radius, u_r is the relative velocity between the bubble and the liquid, κ is the diffusivity of air in water, and C_∞ and C_0 are the concentrations of dissolved gas at a distant point and at the bubble surface. These concentrations are computed using Henry's law, assuming that the partial pressure of dissolved air in the water column is constant at one atmosphere, similar to the assumption made by Hyman [2]. The total source S_k can then be calculated as

$$S_k = \frac{\mathrm{d}m}{\mathrm{d}t}N, \tag{7}$$

where N is the local bubble number density, which can be calculated with an additional hyperbolic equation

$$\frac{\partial N}{\partial t} + \frac{\partial [u_{\mathrm{g},j}N]}{\partial x_j} = 0. \tag{8}$$

Assuming that the bubbles are spherical, the volume fraction and the bubble number density can be used to calculate the bubble radius

$$r_\mathrm{b} = \left(\frac{3\alpha}{4\pi N}\right)^{1/3}. \tag{9}$$

Following assumption 1, all the inertia terms can be neglected in the gas momentum equations. Additionally, the shear stress and Reynolds stress terms in the gas phase are neglected and the pressure is assumed to be the same in the continuous and dispersed phases. Under these conditions, the gas momentum equations are reduced to

$$-\frac{\partial}{\partial x_i}(\alpha p) + \alpha \rho_g g \delta_{i3} + M_{g,i} = 0, \tag{10}$$

where the interfacial momentum sources of the liquid and gas phases are related by

$$M_{g,i} + M_{1,i} = 0, \tag{11}$$

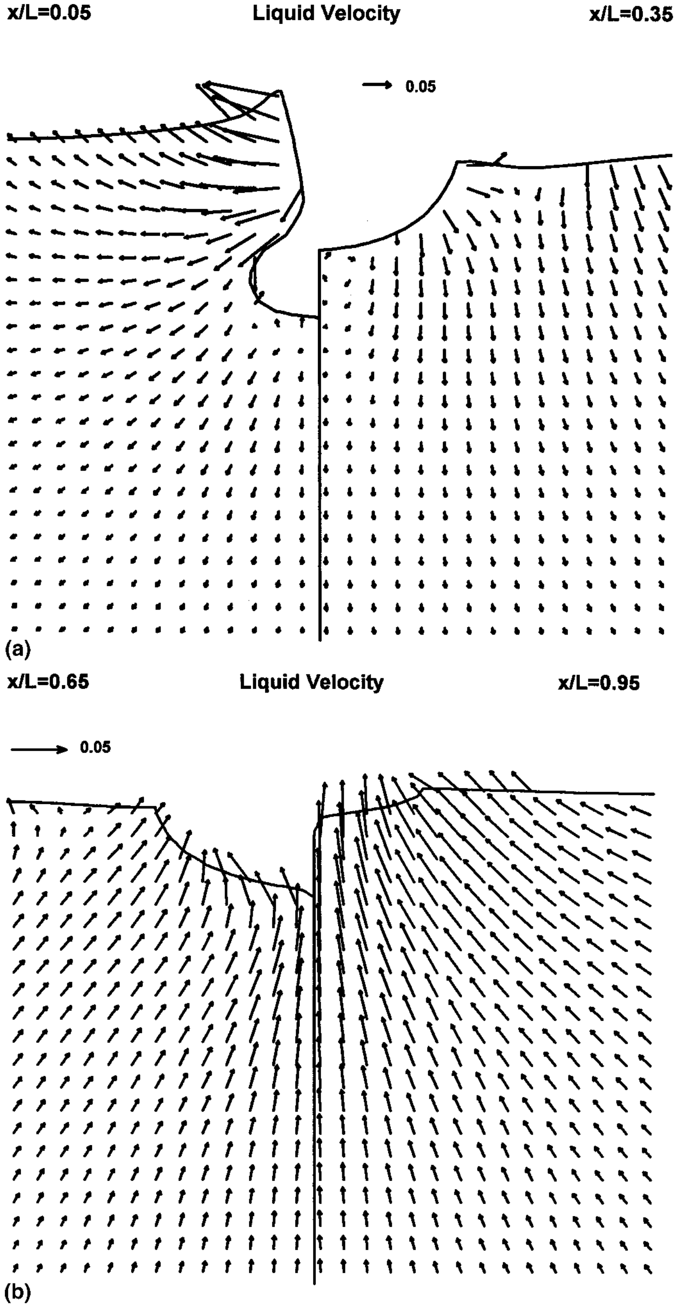

Figure 6. Liquid cross-plane velocity for $x/L = 0.05$, 0.35, 0.65, 0.95, 1.05 and 1.35.

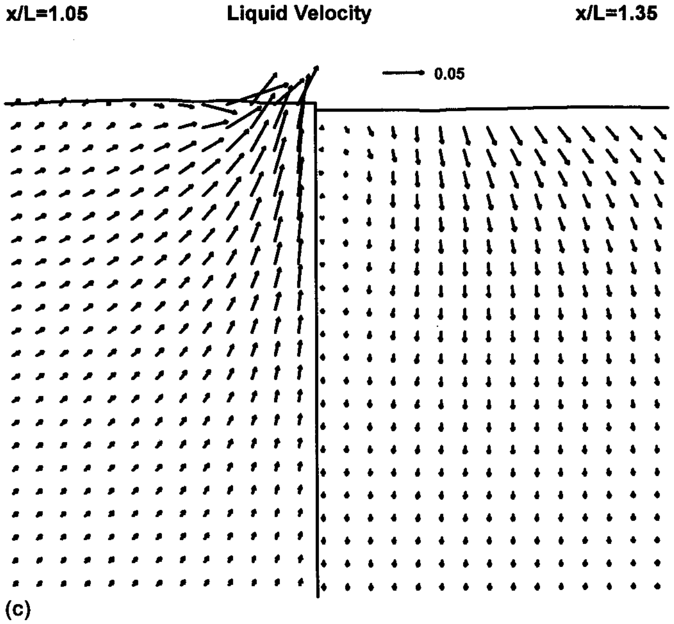

Figure 6 (*Continued*)

then it follows that the liquid momentum equations can be reduced to the two-phase modified RANS equations

$$\frac{\partial u_{1,i}}{\partial t}+u_{1,j}\frac{\partial u_{1,i}}{\partial x_j}+\frac{1}{(1-\alpha)}\frac{\partial}{\partial x_j}[(1-\alpha)\overline{u'_{1,i}u'_{1,j}}]$$
$$=-\frac{1}{(1-\alpha)\rho_1}\frac{\partial p}{\partial x_i}+\frac{\nu}{(1-\alpha)}\frac{\partial}{\partial x_j}\left[(1-\alpha)\left(\frac{\partial u_{1,i}}{\partial x_j}+\frac{\partial u_{1,j}}{\partial x_i}\right)\right]+\frac{(1-\alpha)\rho_1+\alpha\rho_g}{(1-\alpha)\rho_1}g\delta_{i3}, \tag{12}$$

where in the last gravity head term the multiplier is almost one, even for very large gas volume fractions. The third term on the left-hand-side is the Reynolds stress tensor, which can be constituted as

$$-\overline{u'_iu'_j}=\nu_t\left(\frac{\partial u_i}{\partial x_j}+\frac{\partial u_j}{\partial x_i}\right)-\frac{2}{3}\delta_{ij}k. \tag{13}$$

In Equation (13) the eddy diffusivity, ν_t, and the turbulent kinetic energy, k, have been introduced. To calculate the turbulent viscosity, the Baldwin–Lomax algebraic turbulence model [12] was used, modified to account for the effect of the gas in the turbulence quantities. Even though state-of-the-art turbulence modeling for ship hydrodynamics has evolved to include two-equation [13] and full Reynolds-stress [14] models, the Baldwin–Lomax model was chosen here for simplicity. More complex models would have made a better prediction of the single-phase hydrodynamics, the turbulent bubble dispersion and bubble wake diffusion, but the coarse qualitative results of the two-phase flow are expected to be essentially the same. However, it must be noticed that because of its simplicity, the Baldwin–Lomax model is limited in its utility as a predictive tool in ship hydrodynamics and therefore, more complex models must be tested for the case of two-phase flows. In the Baldwin–Lomax model the viscosity is calculated near the wall using the following relationship

$$\nu_{t,\mathrm{w}} = \ell_{\mathrm{m}}^2 |\bar{\omega}|, \tag{14}$$

and in the outer layer with the expression

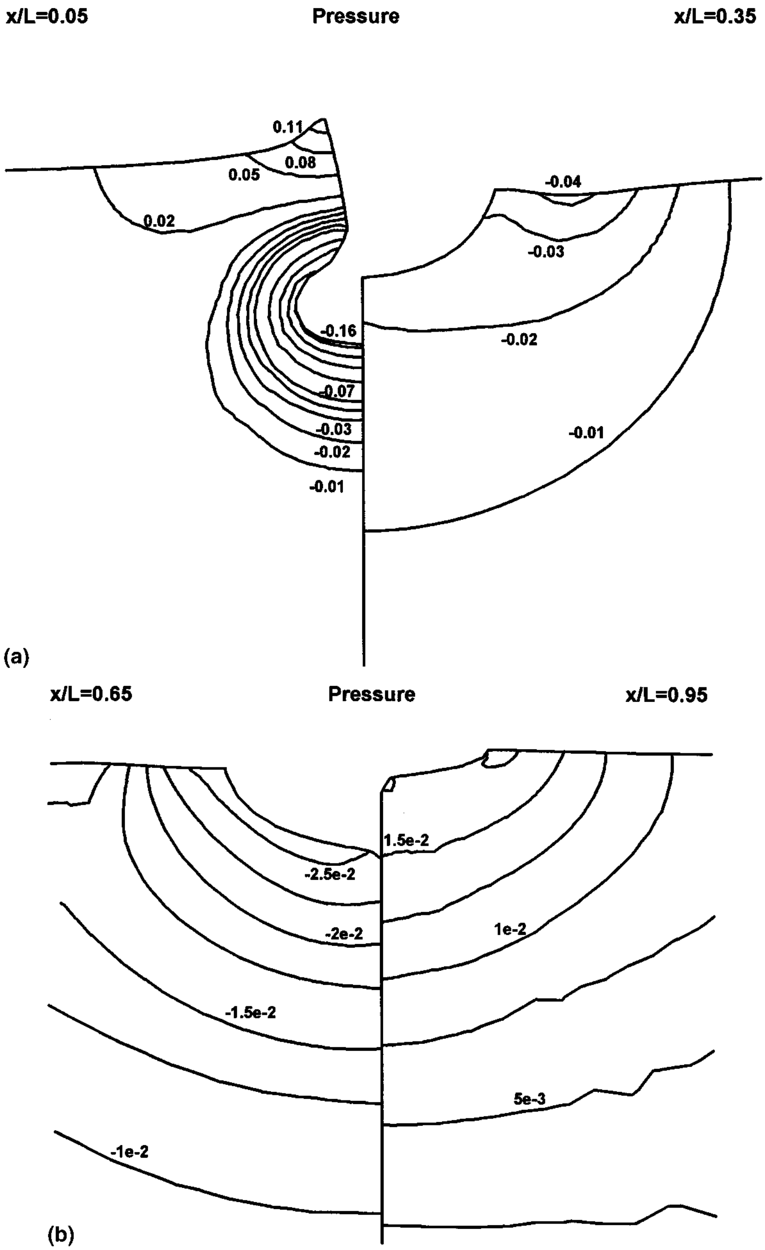

Figure 7. Pressure contour levels at different cross-planes for $x/L = 0.05$, 0.35, 0.65, 0.95, 1.05 and 1.35.

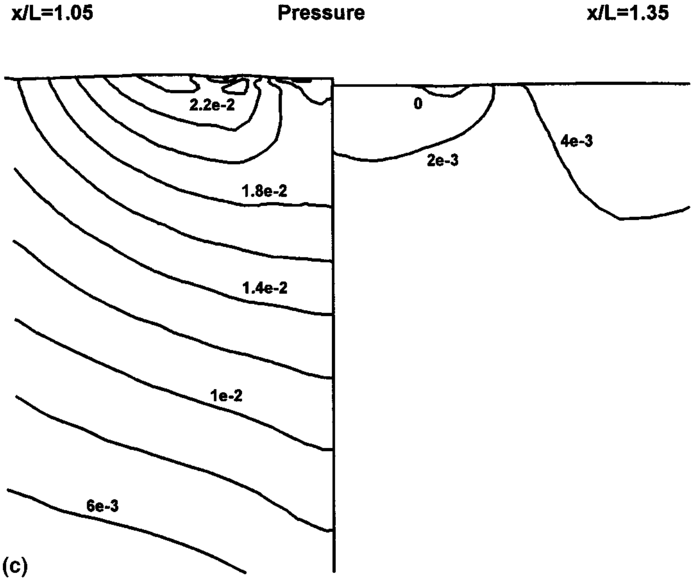

Figure 7 (*Continued*)

$$\nu_{t,\mathrm{o}} = C_k C_{cp} F_{\mathrm{wk}} F_{\mathrm{Kleb}}, \tag{15}$$

where ℓ_{m} is the mixing length, $\bar{\omega}$ is the vorticity, F_{wk} is the wake function, F_{Kleb}, is the Klebanoff intermittence function, and C_k and C_{cp} are empirical constants of the model.

The liquid turbulent kinetic energy is not computed directly from this turbulence model, but can be calculated assuming the following relationship between the mixing length and the eddy viscosity of the $k-\varepsilon$ model

$$k_{\mathrm{l}} = \left(\frac{C_{\ell} \nu_t}{C_{\mu} \ell_{\mathrm{m}}} \right)^2, \tag{16}$$

where $C_{\ell} = 0.4$ and $C_{\mu} = 0.09$ are constants in the $k-\varepsilon$ model. The characteristic length, ℓ_{m} is calculated in the near-hull region as

$$\ell_{\mathrm{m}} = \kappa y \left[1 - \exp\left(-\frac{y^+}{A^+} \right) \right], \tag{17}$$

and is assumed to be

$$\ell_{\mathrm{m}} = F_{\mathrm{wk}} = \min\left(y_{\max} F_{\max}, C_{\mathrm{wk}} y_{\max} \frac{U_{\mathrm{diff}}^2}{F_{\max}} \right) \tag{18}$$

in the outer layer.

Bubble-induced turbulence was modeled with a simple local assumption consistent with the algebraic turbulence model. Following Sato *et al.* [15], bubble-induced turbulence results in an additional turbulent viscosity as

$$\nu_{\mathrm{b}} = 1.2 r_{\mathrm{b}} \alpha |\vec{u}_{\mathrm{r}}|, \tag{19}$$

where $1.2r_{\mathrm{b}}$ is the characteristic length and the relative velocity is the characteristic velocity. Additionally, the total viscosity is calculated using linear superposition [15]

$$\nu_{\text{eff}} = \nu + \nu_t + \nu_{\text{b}}. \tag{20}$$

The influence of bubble-induced turbulence is expected to be important in the near-hull region where relatively large gas volume fractions can be present and the liquid turbulent viscosity is small.

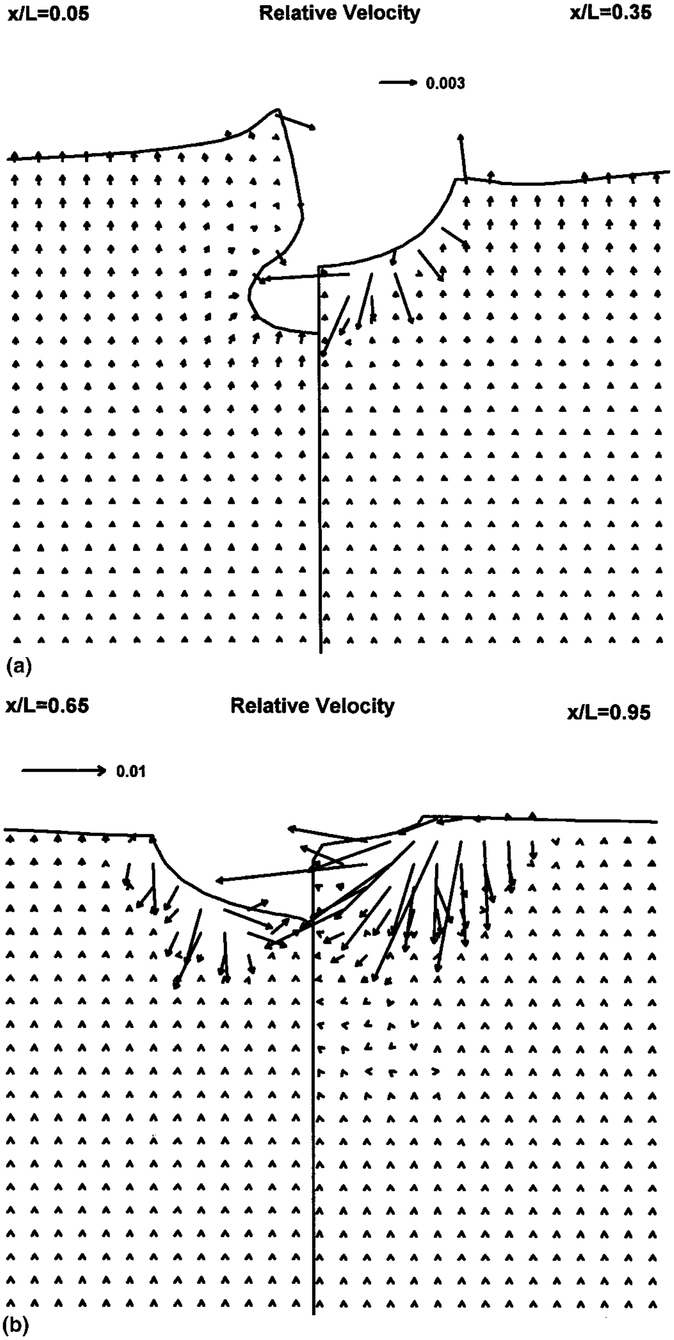

Figure 8. Gas–liquid relative cross-plane velocity for $x/L = 0.05$, 0.35, 0.65, 0.95, 1.05 and 1.35.

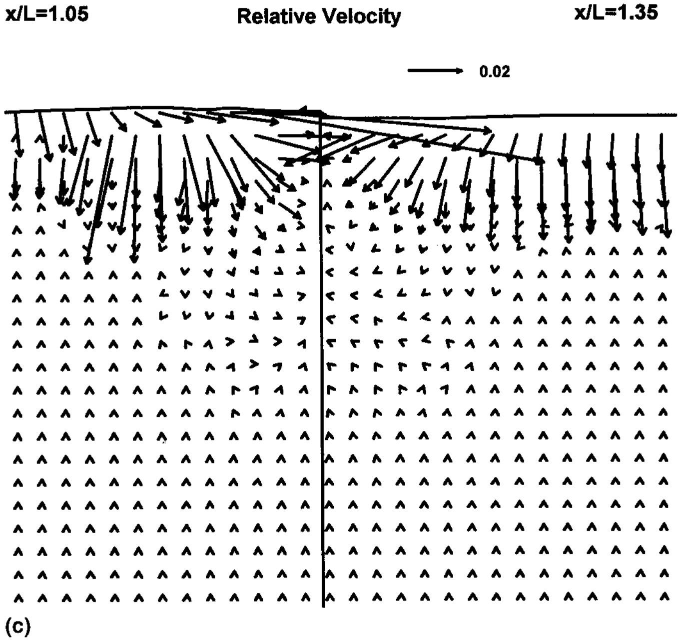

Figure 8 (*Continued*)

The turbulent kinetic energy was also modified to account for the effect of the bubbles. The same linear superposition principle was applied for the bubble-induced kinetic energy, yielding [16]

$$k = k_{1\phi} + k_{\mathrm{b}}, \tag{21}$$

where k_{b} is the turbulent kinetic energy induced by the bubbles and $k_{1\phi}$ is the single-phase turbulent kinetic energy, calculated from Equation (16). This model is considered strictly valid for gas volume fractions of up to $\approx 3\%$. For higher values the interaction between the bubbles would increase the bubble-induced turbulent kinetic energy [16]. The bubble-induced turbulence results in an additional pseudo-turbulent kinetic energy of the form [8]

$$k_{\mathrm{b}} = C_p \alpha (1-\alpha) |\vec{u}_{\mathrm{r}}|^2. \tag{22}$$

Expanding the interfacial momentum sources, the gas phase momentum conservation equation (10) is written as

$$-\frac{\partial(\alpha p)}{\partial x_i} + \alpha \rho_{\mathrm{g}} g \delta_{i3} - p\frac{\partial(1-\alpha)}{\partial x_i} + M_{\mathrm{g},i}^{\mathrm{VM}} + M_{\mathrm{g},i}^{L} + M_{\mathrm{g},i}^{D} + M_{\mathrm{g},i}^{\mathrm{TD}} = 0. \tag{23}$$

In Equation (23) the interfacial momentum transfer terms have been modeled separately. The virtual mass accounts for the effect of acceleration of the liquid displaced by the bubbles, and can be modeled as [7]

$$M_i^{\mathrm{vm}} = \alpha \rho_1 C_{\mathrm{vm}} \left[\left(\frac{\partial u_{1,i}}{\partial t} + u_{1,j} \frac{\partial u_{1,i}}{\partial x_j} \right) - \left(\frac{\partial u_{\mathrm{g},i}}{\partial t} + u_{\mathrm{g},j} \frac{\partial u_{\mathrm{g},i}}{\partial x_j} \right) \right], \tag{24}$$

where the virtual mass coefficient C_{vm}, is 0.5 for dilute potential flow [1]. The lift force term is calculated from potential flow theory, and can be expressed as

$$M_i^L = -\alpha\rho_1 C_L \varepsilon_{ijk}\varepsilon_{klm}(u_{1,j}-u_{\mathrm{g},j})\frac{\partial u_{1,l}}{\partial x_m}. \tag{25}$$

In Equation (25) ε_{ijk} is the third-order permutation tensor and C_L is the lift coefficient, which has been found to be ≈ 0.1 for most practical two-phase flows [17–19].

The drag force is expected to be one of the most important forces in the process due to the small size of the bubbles present in the flow. The drag force may be expressed as

$$M_i^D = \alpha\rho_1 \frac{3}{8}\frac{C_D}{r_{\mathrm{b}}}(u_{1,i}-u_{\mathrm{g},i})|\vec{u}_{\mathrm{r}}|, \tag{26}$$

where C_D is the drag coefficient, which is assumed to be [20]

$$C_D = \frac{12}{Re_{\mathrm{b}}(1-\alpha)}(1+0.168Re_{\mathrm{b}}^{0.75}), \tag{27}$$

where Re_{b} is the bubble Reynolds number based on the bubble radius and the magnitude of the gas–liquid relative velocity, u_{r}. It should be noted that Equation (27) reduces to the Stokes drag coefficient when the bubble Reynolds number is small and the gas volume fraction is negligible.

The last term is the turbulent dispersion which is of major importance in this work, not only because is the cause of bubble dispersion in the wake of the ship, but also because it is the only force that prevents unrealistic gas concentrations at the hull.

Nevertheless, the turbulent dispersion term should show a dispersion behavior for very small bubbles similar to that of passive scalars. This means that the dependence on the radius must be the same as that in the drag term. This fact suggests that the turbulent dispersion coefficient must be a function of the bubble radius and that for very small bubbles the diffusion of bubbles due to the turbulent dispersion must satisfy

$$Sc_{\mathrm{b}} = \frac{\nu_t}{\nu_{\mathrm{b}}} \cong 1, \tag{28}$$

where Sc_{b} is the bubble Schmidt number and ν_{b} is the bubble diffusion. Some evidence [21] shows that for the case of small solid particles the Schmidt number should be between 0.7 and 1. In this limiting case all the forces but the drag and the turbulent dispersion are zero in Equation (23), and the turbulent dispersion force can be calculated as

$$M_i^{\mathrm{TD}} = -\frac{3}{8}\rho_1\frac{C_D|u_{\mathrm{r}}|}{r_{\mathrm{b}}}\frac{\nu_t}{Sc_{\mathrm{b}}}\frac{\partial\alpha}{\partial x_i}. \tag{29}$$

In the case of the flow around a ship, most of the bubbles fall in the range of radius between 10 and 150 μm, with only a few bubbles up to 500 μm [22]. For this reason, the Schmidt number is taken to be one and Equation (29) is considered to be valid over the entire range. Even though much effort has been dedicated to the subject of turbulent dispersion, most of it has been devoted to Lagrangian dispersion models. More research is needed in this area in Eulerian dispersion models.

If assumptions 1 and 3 are used, the non-dimensional piezometric pressure $\hat{p} = p/\rho_1 U_{\mathrm{o}}^2 + \hat{z}/Fr^2$ is introduced, and the system of equations is non-dimensionalized using the ship velocity U_0 and the ship length L, the continuity momentum and number density equations for the liquid and gas phases take on the following dimensionless form.

Liquid continuity equation

$$\frac{\partial(1-\alpha)}{\partial\hat{t}}+\frac{\partial[(1-\alpha)\hat{u}_{1,j}]}{\partial\hat{x}_j}=0. \tag{30}$$

Liquid momentum equation

$$\begin{aligned}&\frac{\partial\hat{u}_{1,i}}{\partial\hat{t}}+\left[\hat{u}_{1,j}-\frac{1}{(1-\alpha)}\frac{\partial}{\partial\hat{x}_j}\left(\frac{1-\alpha}{Re_{\mathrm{t}}}\right)\right]\frac{\partial\hat{u}_{1,j}}{\partial\hat{x}_j}-\frac{1}{(1-\alpha)}\frac{\partial}{\partial\hat{x}_j}\left(\frac{1-\alpha}{Re_{\mathrm{t}}}\right)\frac{\partial\hat{u}_{1,j}}{\partial\hat{x}_i}\\&=-\frac{\partial}{\partial\hat{x}_i}\left(\hat{p}+\frac{2}{3}\hat{k}\right)+\frac{1}{Re_{\mathrm{t}}}\frac{\partial}{\partial\hat{x}_j}\left(\frac{\partial\hat{u}_{1,i}}{\partial\hat{x}_j}+\frac{\partial\hat{u}_{1,j}}{\partial\hat{x}_i}\right)+\frac{1}{1-\alpha}\left[-\frac{\partial}{\partial\hat{x}_i}\left(\hat{p}+\frac{2}{3}\hat{k}\right)+\frac{\alpha\delta_{i3}}{Fr^2}\right].\end{aligned} \tag{31}$$

Gas continuity equation

$$\frac{\partial(\hat{\rho}_{\mathrm{g}}\alpha)}{\partial\hat{t}}+\frac{\partial(\hat{\rho}_{\mathrm{g}}\alpha\hat{u}_{\mathrm{g},j})}{\partial\hat{x}_j}=\frac{\mathrm{d}\hat{m}}{\mathrm{d}\hat{t}}\hat{N}. \tag{32}$$

Gas momentum equation

$$\begin{aligned}&C_{\mathrm{vm}}\left[\left(\frac{\partial\hat{u}_{\mathrm{g},i}}{\partial\hat{t}}+\hat{u}_{\mathrm{g},j}\frac{\partial\hat{u}_{\mathrm{g},i}}{\partial\hat{x}_j}\right)-\left(\frac{\partial\hat{u}_{1,i}}{\partial\hat{t}}+\hat{u}_{1,j}\frac{\partial\hat{u}_{1,i}}{\partial\hat{x}_j}\right)\right]\\&=-C_L\varepsilon_{ijk}\varepsilon_{klm}(\hat{u}_{1,i}-\hat{u}_{\mathrm{g},i})\frac{\partial\hat{u}_{1.1}}{\partial\hat{x}_m}+\hat{C}_D(\hat{u}_{1,i}-\hat{u}_{\mathrm{g},i})|u_{\mathrm{r}}|-\frac{\partial(\hat{p}+2/3\hat{k})}{\partial\hat{x}_i}+\frac{\delta_{i,3}}{Fr^2}-\hat{C}_D|u_{\mathrm{r}}|\frac{\hat{v}_t}{Sc_{\mathrm{b}}}\frac{1}{\alpha}\frac{\partial\alpha}{\partial\hat{x}_i}.\end{aligned} \tag{33}$$

Bubble number density equation

$$\frac{\partial\hat{N}}{\partial\hat{t}}+\frac{\partial[\hat{u}_{1,j}\hat{N}]}{\partial\hat{x}_j}=0. \tag{34}$$

In Equations (30)–(34), the time, velocity, length, gas density, pressure, eddy diffusivity and turbulent kinetic energy were non-dimensionalized as follows

$$\hat{t}=\frac{tU_0}{L},\qquad \hat{u}=\frac{u}{U_0},\qquad \hat{x}=\frac{x}{L},\qquad \hat{\rho}_{\mathrm{g}}=\frac{\rho_{\mathrm{g}}}{\rho_{\mathrm{g},o}},\qquad \hat{p}=\frac{p}{\rho_1U_0^2},\qquad \hat{v}_t=\frac{v_t}{U_0^2},\qquad \hat{k}=\frac{k}{\rho_1U_0^2}, \tag{35}$$

and in Equations (31) and (33) the turbulent Reynolds number, Re_{t}, the Froude number, Fr, and the modified drag coefficient, $\hat{C}_D$, are given by

$$Re_{\mathrm{t}}=\frac{U_{\mathrm{o}}L}{(v+v_t+v_{\mathrm{b}})},\qquad Fr=\frac{U}{\sqrt{gL}},\qquad \hat{C}_D=\frac{3}{8}C_D\frac{L}{r_{\mathrm{b}}}. \tag{36}$$

The turbulent Reynolds number is the effective Reynolds number seen by the numerical scheme and is a function of the position. Note that the bubble Reynolds number appearing in the gas momentum equation can be calculated independently from the ship Reynolds number, so it is possible to define a liquid problem Reynolds number and a gas problem Reynolds number. From this point on in the paper, all the equations will be expressed in non-dimensional form omitting the dimensionless cap for simplicity.

3. COORDINATE TRANSFORMATION

Following the same approach that Stern *et al.* [23] used for single-phase flow calculations, the equations are transformed from the physical domain, having Cartesian co-ordinates (x, y, z), into the computational domain with co-ordinates (ξ, η, ζ). Only the independent variables are transformed, leaving the dependent variables in the original co-ordinates. In the computational domain the computational cells are cubic with sides of unit length. The generalized transformation is fully characterized with the geometric coefficients b_i^j, g_{ij} and f_i and the Jacobian of the transformation J, which are defined as [24]

$$b_l^j = \varepsilon_{lmn} \frac{\partial x_m}{\partial \xi_j} \frac{\partial x_n}{\partial \xi_k}, \tag{37}$$

$$g_{ij} = \frac{1}{J^2} b_m^i b_m^j, \tag{38}$$

$$f_i = \frac{1}{J} \frac{\partial}{\partial \xi_j} (J g_{ij}), \tag{39}$$

$$J = \begin{vmatrix} x_\xi & x_\eta & x_\zeta \\ y_\xi & y_\eta & y_\zeta \\ z_\xi & z_\eta & z_\zeta \end{vmatrix}. \tag{40}$$

The transformation relations were calculated using the conservative form, and are

$$\nabla \cdot \vec{U} = \frac{1}{J} \frac{\partial}{\partial \xi_j} (b_i^j U_i), \tag{41}$$

$$\nabla \phi \big|_i = \frac{1}{J} b_i^j \frac{\partial \phi}{\partial \xi_j}, \tag{42}$$

$$\nabla^2 \phi = g_{ij} \frac{\partial^2 \phi}{\partial \xi_i \, \partial \xi_i} + f_i \frac{\partial \phi}{\partial \xi_i}, \tag{43}$$

$$\frac{\partial \phi}{\partial t} = \frac{\partial \phi}{\partial \tau} - \frac{1}{J} b_i^j \frac{\partial x_i}{\partial \tau} \frac{\partial \phi}{\partial \xi_j}, \tag{44}$$

where ϕ is a generic scalar field. Equations (30)–(34) can be transformed using the relations (41)–(44), yielding

Gas continuity equation

$$\frac{\partial (\rho_{\mathrm{g}} \alpha)}{\partial \tau} + \frac{1}{J} \frac{\partial (\rho_{\mathrm{g}} \alpha \hat{U}_{\mathrm{g},j})}{\partial \xi_j} = \frac{1}{J} b_i^j \frac{\partial x_i}{\partial \tau} \frac{\partial (\rho_{\mathrm{g}} \alpha)}{\partial \xi_j} + N \frac{\mathrm{d}m}{\mathrm{d}t}. \tag{45}$$

Bubble number density equation

$$\frac{\partial N}{\partial \tau} + \frac{1}{J} \frac{\partial (N \hat{U}_{\mathrm{g},j})}{\partial \xi_j} = \frac{1}{J} b_i^j \frac{\partial x_i}{\partial \tau} \frac{\partial N}{\partial \xi_j}. \tag{46}$$

Gas momentum equation

$$
\begin{aligned}
&C_{\mathrm{vm}}\left(\frac{\partial u_{\mathrm{g},i}}{\partial\tau}-\frac{1}{J}b_i^j\frac{\partial x_i}{\partial\tau}\frac{\partial u_{\mathrm{g},i}}{\partial\xi_j}+\breve{U}_{\mathrm{g},j}\frac{\partial u_{\mathrm{g},i}}{\partial\xi_j}\right)\\
&=C_{\mathrm{vm}}\left(\frac{\partial u_{1,i}}{\partial\tau}-\frac{1}{J}b_i^j\frac{\partial x_i}{\partial\tau}\frac{\partial u_{1,i}}{\partial\xi_j}+\breve{U}_{1,j}\frac{\partial u_{1,i}}{\partial\xi_j}\right)-C_L\varepsilon_{ijk}\varepsilon_{klm}(u_{1,i}-u_{\mathrm{g},i})\frac{1}{J}b_m^n\frac{\partial u_{1,1}}{\partial\xi_n}+\hat{C}_D(u_{1,i}-u_{\mathrm{g},i})|\vec{u}_{\mathrm{r}}|\\
&\quad+\frac{\delta_{i,3}}{Fr_{\mathrm{b}}^2}-\frac{1}{J}b_i^j\frac{\partial p}{\partial\xi_j}-\frac{1}{\alpha}\hat{C}_D|u_{\mathrm{r}}|\frac{\hat{v}_t}{Sc_{\mathrm{b}}}\frac{1}{J}b_i^j\frac{\partial\alpha}{\partial\xi_j}.
\end{aligned}
\tag{47}
$$

Liquid continuity equation

$$
\frac{\partial(1-\alpha)}{\partial\tau}+\frac{1}{J}\frac{\partial[(1-\alpha)U_{1,j}]}{\partial\xi_j}=\frac{1}{J}b_i^j\frac{\partial x_i}{\partial\tau}\frac{\partial(1-\alpha)}{\partial\xi_j}.
\tag{48}
$$

Liquid momentum equation

$$
\begin{aligned}
&\frac{\partial u_{1,j}}{\partial\tau}-\frac{b_i^j}{J}\frac{\partial x_i}{\partial\tau}\frac{\partial u_{1,i}}{\partial\xi_j}+\frac{b_n^j}{J}\left(u_{1,n}-\frac{\partial x_n}{\partial\tau}-\frac{1}{(1-\alpha)}\frac{b_n^m}{J}\frac{\partial[(1-\alpha)/Re_{\mathrm{t}}]}{\partial\xi_m}\right)\frac{\partial u_{1,i}}{\partial\xi_j}\\
&-\frac{1}{(1-\alpha)}\frac{b_j^m}{J}\frac{b_i^n}{J}\frac{\partial[(1-\alpha)/Re_{\mathrm{t}}]}{\partial\xi_m}\frac{\partial u_{1,j}}{\partial\xi_n}=-\frac{b_i^j}{J}\frac{\partial}{\partial\xi_j}\left(p+\frac{2}{3}k\right)+\frac{1}{Re_{\mathrm{t}}}g_{kj}\frac{\partial^2 u_{1,i}}{\partial\xi_k\,\partial\xi_j}\\
&+f_j\frac{\partial u_{1,i}}{\partial\xi_j}+\frac{1}{Re_{\mathrm{t}}}\frac{b_i^k}{J^2}\frac{\partial^2\hat{U}_{1,j}}{\partial\xi_k\,\partial\xi_j}+\frac{1}{1-\alpha}\left[-\frac{b_i^j}{J}\frac{\partial}{\partial\xi_j}\left(p+\frac{2}{3}k\right)+\frac{\alpha\delta_{i3}}{Fr^2}\right],
\end{aligned}
\tag{49}
$$

where the contravariant and modified contravariant velocities [25] were introduced and correspond to the velocities in the direction of the transformed co-ordinates and net fluxes perpendicular to transformed surfaces

$$
\breve{U}_i=\frac{1}{J}b_j^iu_j=\frac{1}{J}(b_1^iU+b_2^iV+b_3^iW),
\tag{50}
$$

$$
\breve{U}_i=b_j^iu_j=(b_1^iU+b_2^iV+b_3^iW).
\tag{51}
$$

Equations (45)–(49) constitute the fully coupled two-fluid model in three-dimensional generalized co-ordinates. For gas volume fraction equal to zero the system reduces to the single-phase RANS equations.

4. NUMERICAL METHOD

4.1. Liquid phase conservation equations

For the liquid momentum and mass conservation equations, the CFDSHIP-IOWA code developed by Stern *et al.* [23] and Tahara and Stern [26] was used in a modified form, to account for the presence of gas bubbles as shown in Equations (48) and (49). CFDSHIP-IOWA is currently being used to calculate the steady state flow around the US Navy FF-1052. A brief discussion of the modifications needed to calculate the two-phase flow case is included here; for further details the reader should see the references cited.

The momentum equations were discretized using a 12-point finite-analytic method. The numerical method for the single-phase equations remains unchanged except for the presence several source terms arising from the interaction with gas and from the fact that now the liquid velocity field does not satisfy zero divergence (see the liquid continuity equation). Additionally, the presence of the liquid volume fraction multiplying the stress tensors causes the need of calculation of spatial derivatives of the volume fraction. These are performed using centered differences.

A key point in the coupling between the gas and liquid conservation equations is the treatment of the liquid continuity equation to avoid the unrealistic oscillations that could appear in incompressible calculations. CFDSHIP-IOWA uses the pressure-implicit split-operator (PISO) algorithm. This method allows the calculation of the velocity and the pressure in the same nodes, avoiding the need for staggered grids. The liquid continuity equation is solved in a control volume as shown in Figure 2 and the liquid volume fraction is included to calculate the mass fluxes through the walls of the cell.

The solution procedure for the liquid equations using the PISO algorithm is as follows. First, the momentum equations are solved implicitly using the pressure from the previous time step. Second, the pressure equation is solved implicitly to obtain an intermediate pressure, and the corrected velocity field is solved explicitly to satisfy the continuity equation and the pressure is recalculated. Steady state flows are calculated in this work, therefore, the velocity and pressure fields do not have to be completely converged at each 'time step', allowing a more economical way to reach steady state by making a few iterations of the pressure and momentum equations at each time step. The same principle is applied when solving the equations for the gas phase. Finally, all the equations are solved using a tridiagonal solver and the method of lines.

It must be noticed that due to the bubble-induced turbulence, the effective cell Reynolds number, Equation (36), will generally be smaller in a two-phase flow than in a single-phase flow.

4.2. *Gas phase conservation equations*

Equations (45) and (46) are advection equations, and were solved using a control-volume upwinding approach [27] including in a TVD flux limiter to reduce the artificial numerical diffusivity [28,29]. The resulting scheme is second-order-accurate in 1D advection problems and has the advantage of preventing the development of non-physical spurious oscillations. For multidimensional problems, Leveque and Goodman [30] have shown that the TVD schemes are at most first-order-accurate. However, very good results were obtained with this type of method and in recent years this type of solver has become very popular for solving hyperbolic problems in two or three dimensions (see e.g. Tamamidis and Assanis [31] and Saxena and Ravi [32]).

A control volume in the computational domain is shown in Figure 2. Here, P is a node in the computational grid and the neighboring nodes are north (N), south (S), east (E), west (W), down (D) and up (U). The properties at the faces of the control volume are represented with lower case letters. Integrating Equation (45) or (46) using a simple first-order implicit formulation for the time derivative results in the following scheme

$$\begin{aligned}\frac{\phi_{\mathrm{P}}-\phi_{\mathrm{P}}^{n-1}}{\Delta\tau} &= \max(\hat{V}_{\mathrm{w}},0)[\phi_{\mathrm{W}}+C_{\mathrm{o}}\varphi(r_{\mathrm{w}}^{-})\Delta\phi_{\mathrm{w}}^{-}]+\min(\hat{V}_{\mathrm{w}},0)[\phi_{\mathrm{P}}-C_{\mathrm{o}}\varphi(r_{\mathrm{w}}^{+})\Delta\phi_{\mathrm{w}}^{+}]\\ &\quad -\max(\hat{V}_{\mathrm{e}},0)[\phi_{\mathrm{P}}+C_{\mathrm{o}}\varphi(r_{\mathrm{e}}^{-})\Delta\phi_{\mathrm{e}}^{-}]-\min(\hat{V}_{\mathrm{e}},0)[\phi_{\mathrm{E}}-C_{\mathrm{o}}\varphi(r_{\mathrm{e}}^{+})\Delta\phi_{\mathrm{e}}^{+}]\end{aligned}$$

$$\begin{aligned}
&+\max(\hat{U}_{\mathrm{u}}, 0)[\phi_{\mathrm{U}} + C_{\mathrm{o}}\varphi(r_{\mathrm{u}}^{-})\Delta\phi_{\mathrm{u}}^{-}] + \min(\hat{U}_{\mathrm{u}}, 0)[\phi_{\mathrm{P}} - C_{\mathrm{o}}\varphi(r_{\mathrm{u}}^{+})\Delta\phi_{\mathrm{u}}^{+}]\\
&-\max(\hat{U}_{\mathrm{d}}, 0)[\phi_{\mathrm{P}} + C_{\mathrm{o}}\varphi(r_{\mathrm{d}}^{-})\Delta\phi_{\mathrm{d}}^{-}] - \min(\hat{U}_{\mathrm{d}}, 0)[\phi_{\mathrm{D}} - C_{\mathrm{o}}\varphi(r_{\mathrm{d}}^{+})\Delta\phi_{\mathrm{d}}^{+}]\\
&+\max(\hat{W}_{\mathrm{s}}, 0)[\phi_{\mathrm{S}} + C_{\mathrm{o}}\varphi(r_{\mathrm{s}}^{-})\Delta\phi_{\mathrm{s}}^{-}] + \min(\hat{W}_{\mathrm{s}}, 0)[\phi_{\mathrm{P}} - C_{\mathrm{o}}\varphi(r_{\mathrm{s}}^{+})\Delta\phi_{\mathrm{s}}^{+}]\\
&-\max(\hat{W}_{\mathrm{n}}, 0)[\phi_{\mathrm{P}} + C_{\mathrm{o}}\varphi(r_{\mathrm{n}}^{-})\Delta\phi_{\mathrm{n}}^{-}] - \min(\hat{W}_{\mathrm{n}}, 0)[\phi_{\mathrm{N}} - C_{\mathrm{o}}\varphi(r_{\mathrm{n}}^{+})\Delta\phi_{\mathrm{n}}^{+}] + S_{\phi}, \qquad (52)
\end{aligned}$$

where ϕ can take the value (α, N), $C_{\mathrm{o}} = 0.5$ and all the terms are calculated at 'time' step n, except when indicated by a superscript $n-1$. The gradients in Equation (52) are defined as

$$\begin{aligned}
&\Delta\phi_{\mathrm{e}}^{+} = \phi_{\mathrm{EE}} - \phi_{\mathrm{E}}, \qquad \Delta\phi_{\mathrm{e}}^{-} = \phi_{\mathrm{P}} - \phi_{\mathrm{W}}, \qquad \Delta\phi_{\mathrm{w}}^{+} = \phi_{\mathrm{E}} - \phi_{\mathrm{P}},\\
&\Delta\phi_{\mathrm{w}}^{-} = \phi_{\mathrm{W}} - \phi_{\mathrm{WW}}, \text{ etc.}, \qquad (53)
\end{aligned}$$

and the flux limiter function is the 'superbee' compressive transfer function of Roe [29]

$$\varphi(r) = \max[0, \min(2r, 1), \min(r, 2)], \qquad (54)$$

where r is the ratio of consecutive gradients and is defined as

$$r_{\mathrm{e}}^{-} = \frac{\phi_{\mathrm{E}} - \phi_{\mathrm{P}}}{\alpha_{\mathrm{P}} - \alpha_{\mathrm{W}}}, \qquad r_{\mathrm{e}}^{+} = \frac{\phi_{\mathrm{P}} - \phi_{\mathrm{W}}}{\phi_{\mathrm{E}} - \phi_{\mathrm{EE}}}, \qquad r_{\mathrm{w}}^{-} = \frac{\phi_{\mathrm{P}} - \phi_{\mathrm{W}}}{\phi_{\mathrm{W}} - \phi_{\mathrm{WW}}}, \qquad r_{\mathrm{w}}^{+} = \frac{\phi_{\mathrm{W}} - \phi_{\mathrm{P}}}{\phi_{\mathrm{P}} - \phi_{\mathrm{E}}}, \text{ etc.} \qquad (55)$$

The implementation of the flux limiter has a considerably high computational cost, but the numerical diffusion introduced by the full upwind scheme yielded unacceptable results. Another drawback of the TVD scheme is that it is less robust than the full upwind scheme, resulting in convergence difficulties. To avoid these problems, the deferred correction source provided by the limiter was reduced, using a constant $C_{\mathrm{o}} = 0.49$ instead of 0.5. Note that for $C_{\mathrm{o}} = 0$ the full upwinding scheme is recovered (i.e. no correction fluxes are applied).

In contrast to the case of the gas continuity equation and the bubble number density equation, numerical diffusion is not important in the gas momentum equations because the advection term is small and the sources are dominant for the bubble sizes involved. In this case, the numerical method implemented is full upwinding

$$\begin{aligned}
\frac{\phi_{\mathrm{P}} - \phi_{\mathrm{P}}^{n-1}}{\Delta t} &= (\phi_{\mathrm{P}} - \phi_{\mathrm{W}})\max(\hat{V}_{\mathrm{w}}, 0) + (\phi_{\mathrm{P}} - \phi_{\mathrm{E}})\min(\hat{V}_{\mathrm{e}}, 0) + (\phi_{\mathrm{P}} - \phi_{\mathrm{U}})\max(\hat{U}_{\mathrm{u}}, 0)\\
&+ (\phi_{\mathrm{P}} - \phi_{\mathrm{D}})\min(\hat{U}_{\mathrm{d}}, 0) + (\phi_{\mathrm{P}} - \phi_{\mathrm{S}})\max(\hat{W}_{\mathrm{s}}, 0) + (\phi_{\mathrm{P}} - \phi_{\mathrm{N}})\min(\hat{W}_{\mathrm{n}}, 0) + S_{\phi}, \qquad (56)
\end{aligned}$$

where ϕ represents each component of the gas velocity vector. Since the sources are dominant, great care was taken in the implementation of these equations to avoid a too-stiff behavior and allow good convergence rates. It should be noted that the sources can be separated into the terms that are dependent on the gas velocity and those that are independent of the gas velocity. The terms that depend on the gas velocity are the drag force, the lift force, and the turbulent dispersion. To make the matrix system more diagonally dominant and reduce the oscillations in the source during the gas momentum iterations, the source was partitioned as

$$S_{\phi} = S_{\mathrm{i}} + S_{\mathrm{p}}\phi_{\mathrm{p}}, \qquad (57)$$

where S_{i} is the source independent of the solution at point P and S_{p} is the coefficient of the source part dependent on P. Note that S_{p} is also dependent on the solution at point P through the drag term, Equation (26), and through the induced turbulent kinetic energy, Equation (21).

5. COMPUTATIONAL DOMAIN, GRIDS AND BOUNDARY CONDITIONS

The FF-1052 is a Navy frigate which is 126.7 m long with a transom stern and a bulbous bow to accommodate the sonar. The speed used for calculations was 27 knots, which results in full-scale Reynolds and Froude numbers of $Re = 2 \times 10^9$ and $Fr = 0.39$. The computational conditions for the liquid are full Froude number and $Re = 2 \times 10^6$. This low Reynolds number was chosen to allow the use of rather coarse grids and to obtain reasonable results. To calculate higher Reynolds numbers it is necessary to refine the grid [3]. However, for the gas equations the full-scale Reynolds number was used.

Referring to Figure 3, the solution domain extends from $x/L = -0.4$ to 2 and up to a radial distance from the axis $r/L = 1$. As the case is symmetrical with respect to the centerplane, only half of the domain must be calculated. To accommodate the abrupt change at the transom stern, a two-block approach was implemented.

The boundary conditions for the liquid and gas at the different boundaries in the physical domain are

- At the inlet, $x/L = -0.4$: it is assumed that the inlet is far enough from the bow of the ship so that free stream conditions may be used. The liquid velocities and pressure gradient are set to:

  $$u_l = u_g = 1, \qquad v_l = v_g = 0, \qquad w_l = w_g = 0, \qquad \frac{\partial p}{\partial x} = 0. \tag{58}$$

  For the gas volume fraction and bubble number density, an estimation of background entrained air due to wind-induced breaking waves were used, following the measurements made in the North Atlantic by Melville *et al.* [33] for 12.7 m s^{-1} average wind speed. Their results show a gas volume fraction vertical distribution that fits well with a z^{-m} trend where m is somewhere between 2.5 and 3. In this work the volume fraction at the inlet followed the relationship:

  $$\alpha(x = -0.4L, y, z) = \frac{1.6 \times 10^{-4}}{(0.1 + \Delta z)^{2.5}(1 + 0.1\Delta z)}, \tag{59}$$

  where Δz is the depth measured vertically from the free surface. Equation (59) has the same trend as the data of Melville but shows a slightly higher volume fraction, possibly due to wilder sea conditions. The bubble number density is estimated using Equation (9) along with a constant bubble mass of 2.28×10^{-12} kg, corresponding to bubbles with 75 μm radius at the sea surface, a typical size found at the maximum of the bubble size distributions observed in typical wind breaking waves [22,34]. The measurements of Melville *et al.*, were performed from 0.69 to 6.94 m depth, so extrapolation was used to estimate the volume fraction at the sea surface. No information seems to be available for the change of the gas volume fraction in the near surface region, so the same relation (59) trend was used, resulting in a gas volume fraction at the free surface of about 5%. It must be noted that bubbles were not allowed to regenerate (i.e. re-enter the solution domain), so gas is steadily disappearing through the free surface and dissolving as we move to the end of the computational domain.
- At the exit, $x/L = 2$: for the liquid, zero gradient conditions were used

  $$\frac{\partial u_l}{\partial x} = \frac{\partial v_l}{\partial x} = \frac{\partial w_l}{\partial x} = \frac{\partial p}{\partial x} = 0, \tag{60}$$

and for the gas equations, free flux conditions were used.

- At the hull and centerplane, $\eta = 0$ and $\zeta = 0$: solid wall (hull) or symmetry conditions (centerplane), there was no gas or momentum flux. For the liquid equations the conditions were:

$$u_l = 0, \qquad v_l = 0, \qquad w_l = 0 \quad \text{(hull)}, \tag{61}$$

$$\frac{\partial u_l}{\partial y} = \frac{\partial w_l}{\partial y} = \frac{\partial p}{\partial y} = v_l = 0 \quad \text{(centerplane)}. \tag{62}$$

- Outer boundary, at $\eta = \eta_{\max}$, free flow for the gas. For the liquid equations

$$u_l = 1, \qquad v_l = 0, \qquad p = 0,$$

$$u_l \frac{\partial(1-\alpha)}{\partial x} + \frac{\partial(1-\alpha)v_l}{\partial y} + \frac{\partial(1-\alpha)w_l}{\partial z} = 0. \tag{63}$$

- At the free surface: the bubbles are free to leave the control volume. The turbulent dispersion is set to zero to avoid unrealistic loss of bubbles or entrance of air. For the liquid, the model of Stern *et al.* [23] was used, where an exact non-linear free-surface kinematic equation was solved:

$$\frac{\partial \varsigma}{\partial t} + u_l \frac{\partial \varsigma}{\partial x} + v_l \frac{\partial \varsigma}{\partial y} - w_l = 0, \tag{64}$$

and an approximate dynamic free-surface condition is as follows:

$$p = \frac{\varsigma}{Fr^2}. \tag{65}$$

For details about the solution method for the free surface equations the reader is referred to the work of Stern *et al.* [23].

- At the interface between the two blocks, a parametrically-mapped bilinear-interpolation scheme was used to interpolate all the dependent variables in the overlapping planes in each block [23].

The free gas flux boundary conditions were specified using the standard control volume approach in which the flux at the free flow surface is calculated using the values at the center of the control volume. For instance, if the free flow surface is given by $\zeta = \zeta_{\max}$, the balance equation for $\phi (\phi = \alpha, N, u_g, v_g, w_g)$ in one control volume at $\zeta_{\max}$ reads

$$C_P \phi_P = \sum_{k = \mathrm{u,d,e,w,s}} C_k \phi_k + C_n \phi_P + S_{\phi,P}. \tag{66}$$

The condition of no gas or momentum flux was calculated by setting the flow through the appropriate control volume face equal to zero. For example, at the hull or centerplane ($\eta = 0$) the west face must have zero convection, so this was specified as

$$C_P \phi_P = \sum_{k = \mathrm{u,d,e,s,n}} C_k \phi_k + S_{\phi,P}. \tag{67}$$

To study grid convergence, four grids were used, with 78 × 21 × 22 (very coarse), 110 × 21 × 22 (coarse), 110 × 31 × 22 (medium) and 110 × 40 × 40 (fine) nodes in the ξ-, η- and ζ-directions. An overview of the grids is shown in Figure 3. H-grid topology is used. For each

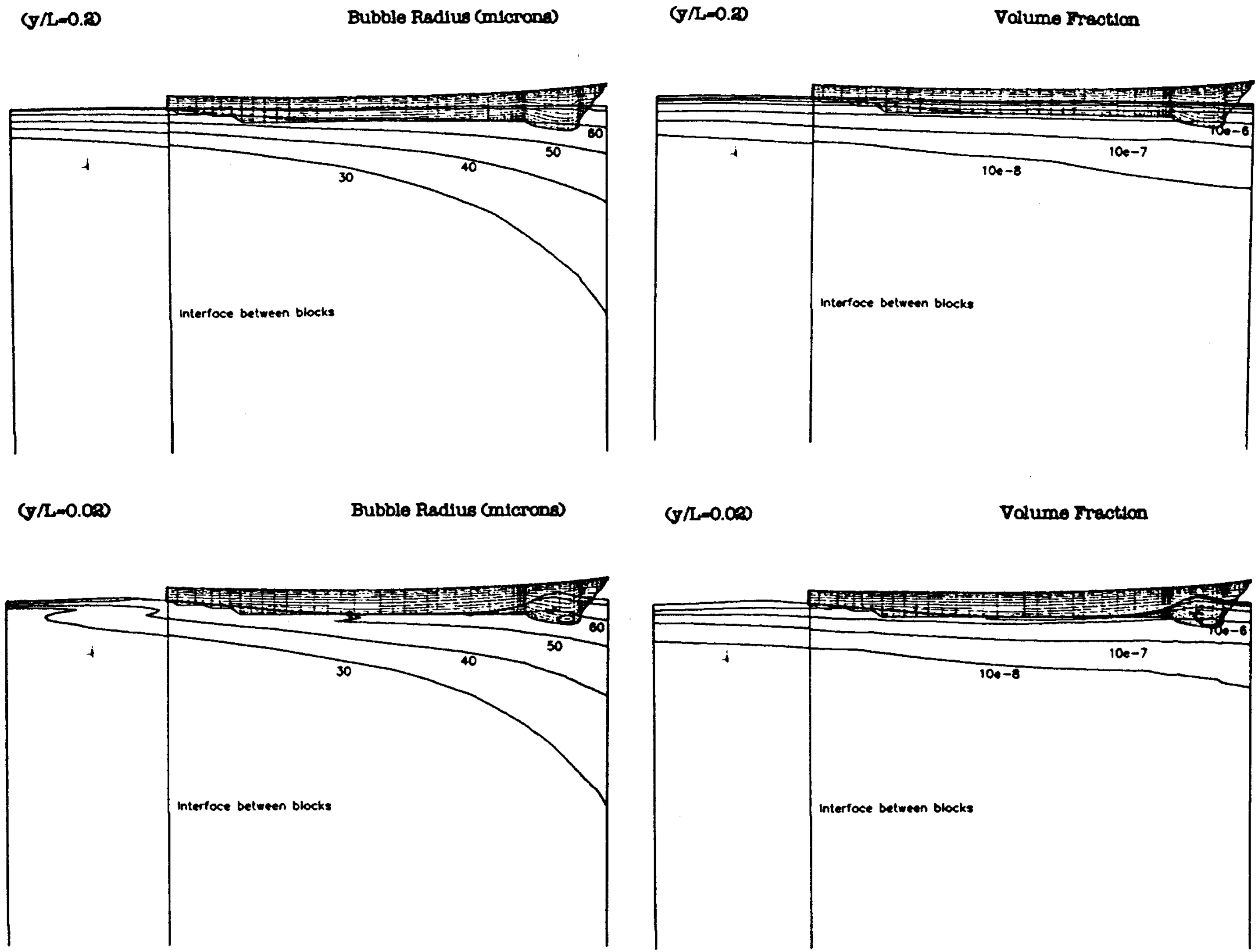

Figure 9. Bubble radius (left) and gas volume fraction (right) at axial vertical planes for $y/L = 0.2$ and 0.02.

grid the first row of nodes is located within $y^+ < 2$, according to the Baldwin–Lomax turbulence model. All the results are shown for the fine grid case. An independent grid for the free surface boundary conditions is used with the same size for all the cases (460 × 100 nodes).

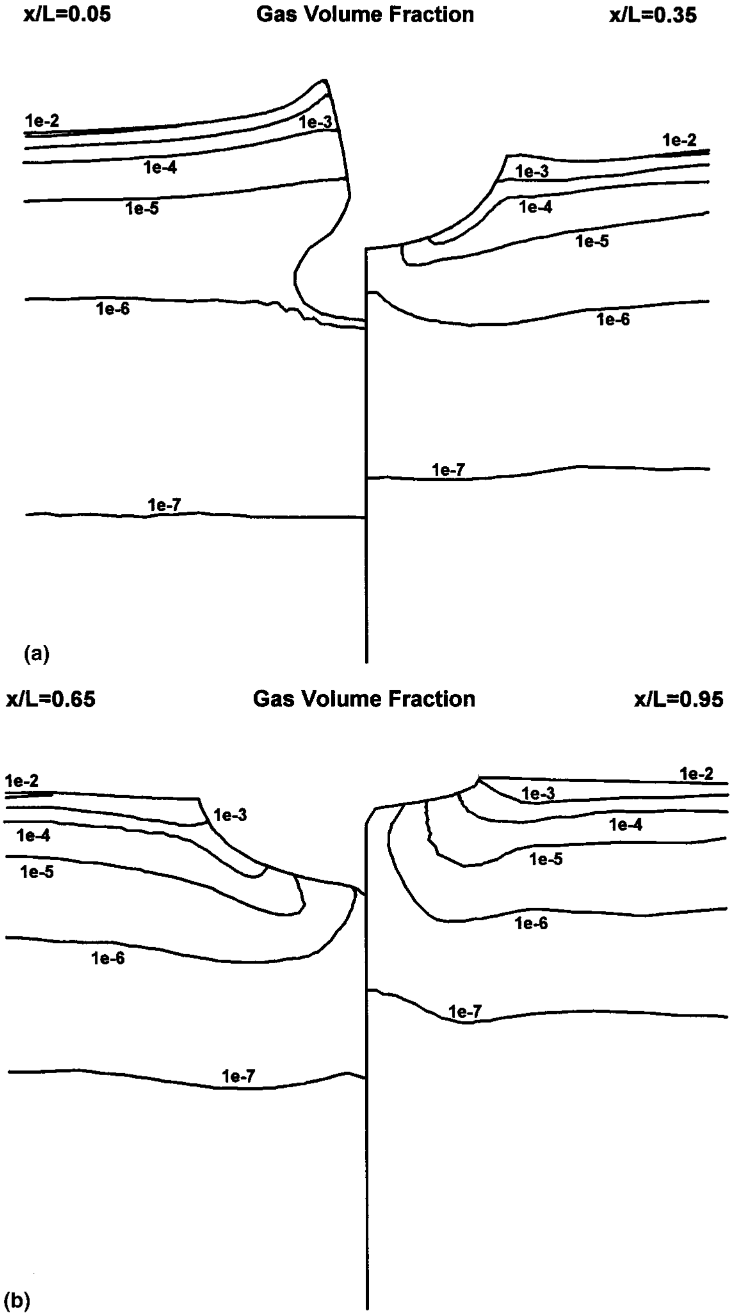

Figure 10. Gas volume fraction at different cross-planes for $x/L = 0.05$, 0.35, 0.65, 0.95, 1.05 and 1.35.

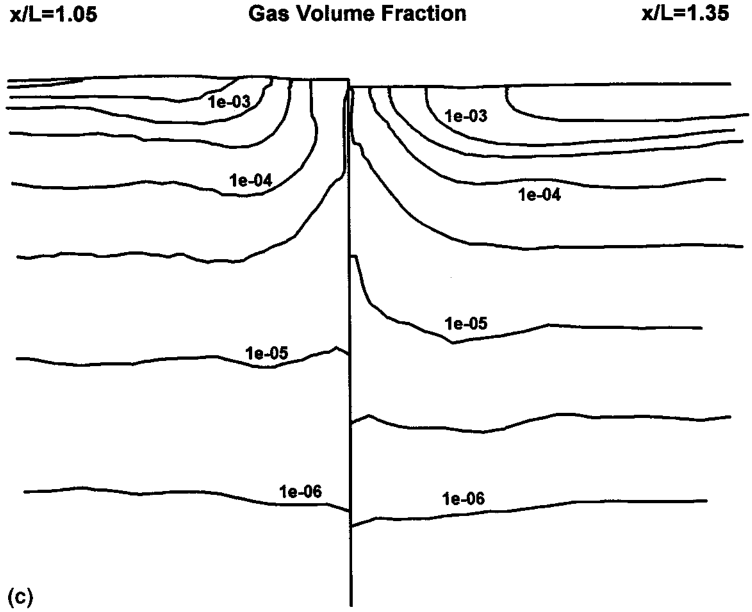

Figure 10 (*Continued*)

6. SOLUTION PROCEDURE

An appropriate solution strategy for the model is to begin by solving the zero volume fraction liquid field and calculate the gas transport assuming the velocity field is known, then iterate to solve the fully coupled model. To obtain an initial solution of the uncoupled liquid field it was often necessary to attain convergence with the fully coupled model, and is convenient to save computational time.

Based on this strategy, the uncoupled pressure and velocity fields for the liquid were calculated first. These fields were used for input in the two-fluid model for the gas velocity, bubble number density and gas volume fraction calculations.

The system of equations was solved iteratively using a pseudo-temporal approach to reach steady state. To achieve convergence it was necessary to underrelax the system with underrelaxation constants of ≈ 0.1 for the liquid momentum equations, 0.01 for the pressure equation, 0.03 for the gas momentum equations and 0.3 for the bubble number density and gas continuity equations. The 'time' step used for the gas equations was 100 times larger than that for the liquid equations, typically $\tau = 0.01$ for the liquid equations and $\tau = 1$ for the gas equations. A significant improvement in the convergence rate was observed by doing this.

A variable was considered converged when the L_2 change indicator between two time steps falls three or more orders of magnitude, where the L_2 norm is defined as

$$L_2 = \frac{\sum_{(i,j,k)=0}^{(i,j,k)_{\max}} |\phi_{i,j,k} - \phi_{i,j,k}^{n-1}|^2}{\text{total number of nodes}}, \tag{68}$$

where indexes i, j and k represent the number of nodes associated with the position (ξ, η, ζ) in the computational domain. The maximum gas volume fraction at the hull and the position at which this is located are also good indicators for convergence and are used together with

Equation (68). The medium case presented here ran in about 6 h on a Cray C90 with memory requirements of 10 megawords. The fine case was run on a Silicon Graphics Power Challenge machine.

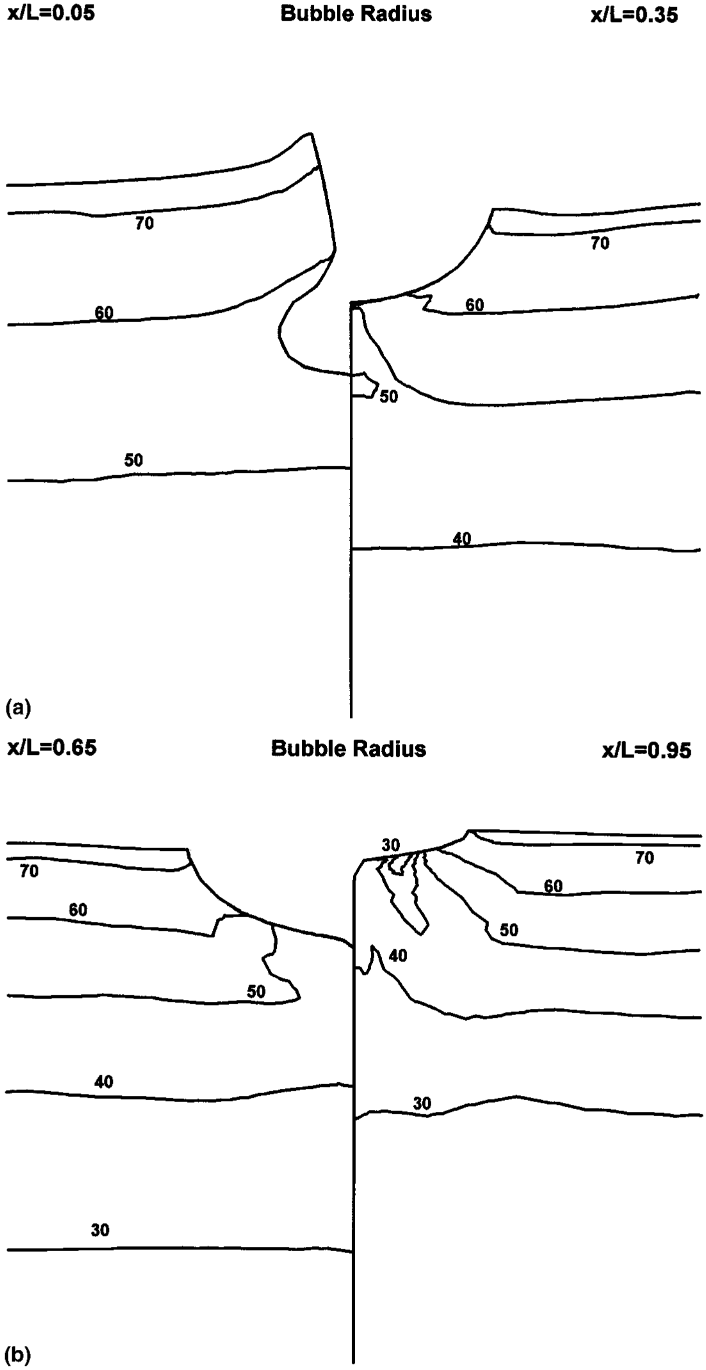

Figure 11. Bubble radius at different cross-planes for $x/L = 0.05$, 0.35, 0.65, 0.95, 1.05 and 1.35.

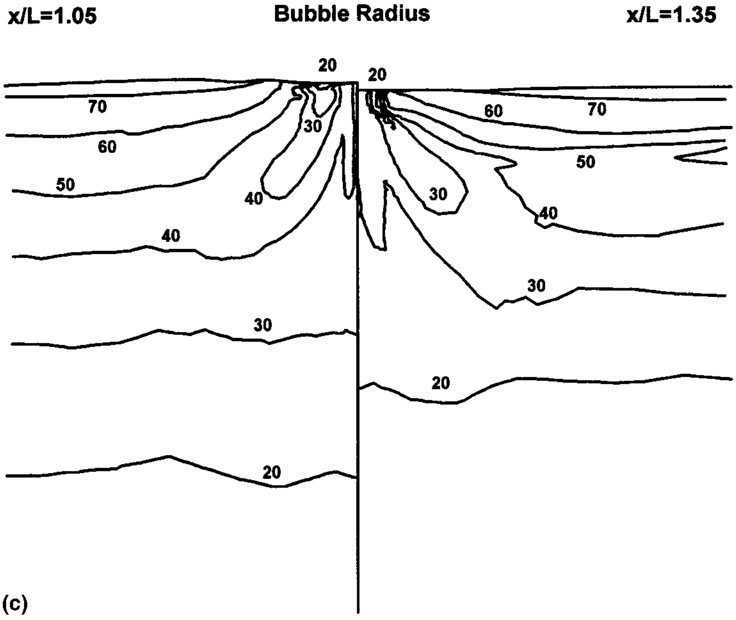

Figure 11 (*Continued*)

7. NUMERICAL RESULTS AND DISCUSSION

A general view of the FF-1052 frigate and the free surface is shown in Figure 1. The contour lines represent constant gas volume fraction, and it is clear from this figure that the influence of the ship causes strong modification of the bubble field in the wake.

Table I shows some integral quantities used for grid convergence analysis. The values shown in each cell are for the very coarse, coarse, medium and fine grids. The quantities chosen are the maximum and minimum pressure and wave height at the hull, the maximum gas volume fraction and bubble number density at the hull, the maximum gas velocity vector in all the domain, and the position of each of these quantities. The bubble number density shown is non-dimensionalized with the reference bubble volume, corresponding to a reference bubble radius of 75 μm. The very coarse grid is too coarse and fails when trying to accommodate the free surface, which causes important misestimations in the volume fraction and number density maxima and their positions. In the other grids the numerical results tend to converge when the grid is refined, but finer grids would probably be necessary to assess complete grid convergence.

Figure 4 shows a comparison between the free-surface wave elevation at the hull of the four grids and the experimental data [4] taken at $Fr = 0.39$, $Re = 2.01 \times 10^7$. Also included is a single-phase calculation with the code CFDSHIP-IOWA at $Fr = 0.39$, $Re = 4.0 \times 10^6$ in a grid with 330720 nodes. It must be noted that the model was allowed to sink and trim in the experiments, which is not allowed in the calculations. In order to compare properly with the numerical calculations, the experimental data was corrected by subtracting the height corresponding to sinkage and trim; see the discussion in the work by Stern *et al.* [23]. Notice that even though *Fr* is the same in all the plots, *Re* changes significantly, therefore differences can be expected. Additionally, the sinkage and trim allowed in the experiments change the wetted geometry, introducing additional differences. However, for the purposes of a qualitative comparison the data available is used. It can be seen that the height and position of the bow peak is correctly predicted, but the second peak at $x/L = 0.32$ and the wave depression at $x/L = 0.6$ are lacking. This is probably due to the low *Re* number used in the calculations, because this feature develops at higher *Re*, as already noticed by Stern *et al.* [23]. On the other hand, it can be clearly seen that the very coarse grid fails to follow the free surface, but the other three grids give essentially the same wave.

For the purposes of this work the fine grid is considered good enough for the calculations.

7.1. Velocity and pressure fields

The U-component contour lines and the (V, W) vectors of the liquid velocity, and pressure contour lines are shown in Figures 5–7, for non-dimensional axial lengths $x/L = 0.05$, 0.35, 0.65, 0.95, 1.05 and 1.35. The single-phase liquid and pressure fields for the frigate with non-zero Froude number are discussed extensively in the works of Paterson *et al.* [3] and Stern *et al.* [23] and are mentioned in this work when appropriate. It must be noted that all the vector fields were interpolated onto uniform grids to allow easier visualization. Otherwise the strong concentration of nodes at the hull makes it difficult to see the results in that region.

The gas–liquid relative velocity vector fields for axial lengths $x/L = 0.05$, 0.35, 0.65, 0.95, 1.05 and 1.35 are shown in Figure 8. Due to the very small size of the bubbles being considered and the nature of the problem, the relative velocities between the gas and the liquid are much smaller than the liquid velocity. Nevertheless, the relative velocity plays a major role in the bubble distribution, mainly because of the lateral lift and the fact that the gas velocity field has non-zero divergence, thus allowing the concentration or depletion of bubbles in certain regions of the flow. Also, due to the presence of bubbles, the liquid velocity is modified resulting in an additional cause for a non-solenoidal gas velocity field. All this is valid close to the ship where the liquid velocity field is highly rotational. Far from the ship, in the inviscid flow region, only the gravitational dispersion and the drag forces are of importance.

At $x/L = 0.05$ the boundary layer is starting to form and the liquid flow is almost irrotational in the plane, except very close to the wall. Nevertheless, the relative velocity field presents complex features. As shown in Figure 8, bubbles tend to move towards the hull at $x/L = 0.05$, where the boundary layer is starting to develop and the velocity gradient is very strong. This causes the lift force to dominate in that region. As the pressure decreases in this region as x increases, the liquid travels faster than the gas and the life force points toward the hull. In general, the opposite occurs for $x/L > 0.5$, where the lift forces repels bubbles from the hull in most of the domain. The (V, W) vectors show the effect of the bubble size on the vertical velocity, which increases close to the surface where the bubbles are bigger, and the strong effect of the turbulent dispersion at the crest of the wave. If we note in Equation (33) that this force has the same order of magnitude as the drag force, the turbulent dispersion force can be expected to be dominant where the gas volume fraction gradients are large. This effect is clearer at $x/L = 0.95$ or larger (see Figure 7), at the cut planes downstream where strong gradients are developing and the turbulent viscosity increases strongly due to the appearance of large scale eddies, mainly in the wake. In this region, the Baldwin–Lomax turbulence model used is less reliable and likely to cause misestimations of the turbulent viscosity, resulting in unrealistic turbulent dispersion.

7.2. Bubble size and gas volume fraction

The general trend followed by the gas volume fraction and the bubble radius in the axial direction is shown in Figure 9. At constant depth there is a loss of gas due to dissolution of the bubbles and convection towards the surface. At greater depths, the dissolution effect is the most important, because of the high pressure that causes the air concentration in the liquid at the bubble surface to increase considerably and the bubble radius to shrink (see Equation (6)). The behavior of the bubble radius and volume fraction far from the ship can be seen for $y/L = 0.2$, where both the effects of hydrostatic pressure and dissolution near the free stream can be observed. Close to the ship, at $y/L = 0.02$, the effects of the ship on the bubble radius are evident. The bubble radius is reduced due to the presence of the ship, which in turn causes the bubbles to stay in the water longer and then dissolve more than the bubbles far from the ship. The dissolution of bubbles competes with the accumulation of bubbles close to the hull to determine the volume fraction behind the ship.

Contour lines of the gas volume fraction and bubble radius for perpendicular planes at $x/L = 0.05$, 0.35, 0.65, 0.95, 1.05 and 1.35 are shown in Figures 10 and 11. At $x/L = 0.05$ almost no bubble accumulation is observed as the flow is close to irrotational, but the gas volume fraction at the surface is smaller close to the ship. At $x/L = 0.35$ some bubble accumulation is observed at the hull and the bubble radius is also affected by the presence of the ship. At $x/L = 0.65$ the reduction in the radius is more noticeable, also causing a reduction of the gas volume fraction in the lower part of the ship, with some gas accumulation persisting at the midgirth where the dissolution effects are smaller. Down to $x/L = 0.95$, dissolution dominates the picture, and even when the bubble concentration at the hull is larger, the gas volume fraction is smaller. This results in the generation of a depleted bubbly wake with very small bubbles, as can be seen at $x/L = 1.05$ and 1.35. Another effect that contributes to the generation of the depletion of gas at the near wake is the generation of a upwelling plume that brings up the smaller bubbles present at deeper positions. This effect has already been observed for the case of temperature stratification [3] and in general is strongly dependent on the ship's geometry and propeller.

8. CONCLUSIONS AND RECOMMENDED FUTURE WORK

A multidimensional computational model for the two-phase flow around a naval surface ship has been presented. The model can calculate the monodispersed gas volume fraction and bubble radius, including the coupling of the gas in the liquid equations. The model was applied to the case of the scavenging of background bubbles in the ocean by a naval surface ship, resulting in the generation of a gas-depleted bubbly wake of small bubbles.

It is important to note the monodisperse property of the model used. Even though the changes in the bubble radius with position and time can be calculated, there is a single bubble size at each position. The case calculated can be simulated in towing-tank conditions, by injecting a single-size bubble population in front of the model ship. However, the single bubble size assumption is an obvious limitation for calculating more realistic cases for full size ships in real sea background, where bubbles enter the water with a size distribution and can break-up, coalesce or collide.

The ultimate goal of this research is to have a reliable model to calculate the bubble concentration and size distribution at each point in time and space in the near field around a ship. Future needs to accomplish this goal are coupling the wave calculation to bubble entrainment by wave breaking and spilling, the introduction of a polydisperse bubble transport model, the calculation of the effect of the propeller including the bubble sources it introduces and improvement of the calculation of the turbulence field, particularly in the wake, where errors on the estimation of the turbulent dispersion were observed. Experimental data to properly assess the accuracy of the model are also necessary.

ACKNOWLEDGMENTS

The help provided by Dr. Eric G. Paterson and Professor Fred Stern of the Institute of Hydraulic Research of the University of Iowa is deeply appreciated. They provided us with grid generation programs for the FF-1052 and the original version of the code CFDSHIP-IOWA that we used as starting point in this work and was modified to serve as the continuous phase solver. This research was sponsored by the Office of Naval Research under Grant N0001-91-J1271; Dr. Edwin Rood was the technical monitor. The computations were performed on the Cray C90 supercomputer at the Naval Oceanographic Supercomputer Center.

REFERENCES

1. R.T. Lahey Jr. and D.A. Drew, 'The current state-of-the-art in modeling of vapor/liquid two-phase flows', *ASME Paper 90-WA/HT-13*, 1990.
2. M. Hyman, 'Modeling ship microbubble wakes', *CSS/TR-94/39*, 1994.
3. E.G. Paterson, M. Hyman, F. Stern, P.M. Carrica, F. Bonetto, D.A Drew and RT. Lahey Jr., 'Near and far-field CFD for a naval combatant including thermal-stratification and two-fluid modeling', *Proc. of the 21st Symposium on Naval Hydrodynamics*, Trondheim, Norway, June 1996.
4. E.E. West, 'Resistance characteristics and appendage orientation data for DE 1052 represented by model 4989', *DTNSRDC/SPD-C-011_H01*, Unclassified 3/13/81, 1964.
5. W.G. Day and R.B. Hurwitz, 'Propeller-disk wake survey data for model 4989 representing the FF 1052-class ship in a turn and with a bass dynamometer boat', *DTNSRDC/SPD-01121*, 1980.
6. T. Rattcliffe and W.T. Lindenmuth, 'Kelvin-wake measurements obtained on five surface ship models', *DTRC-89/038*, 1990.
7. D.A. Drew and R.T. Lahey Jr., 'Application of general constitutive principles to the derivation of multidimensional two-phase flow equations', *Int. J. Multiphase Flow*, **5**, 243 (1979).
8. G.S. Arnold, 'Entropy and objectivity as constraints upon constitutive equations for two fluid modeling of multiphase flow', *Ph.D. Thesis*, Rensselaer Polytechnic Institute, Troy, New York, 1988.
9. J.W. Park, 'Void wave propagation in two-phase flow', *Ph.D. Thesis*, Rensselaer Polytechnic Institute, Troy, New York, 1992.
10. A. Alajbegovic, 'Phase distribution and turbulence structure for solid/fluid upflow in a pipe', *Ph.D. Thesis*, Rensselaer Polytechnic Institute, Troy, New York, 1994.
11. V.G. Levich, *Physiochemical Hydrodynamics*, Prentice-Hall, New York, 1962.
12. B.S. Baldwin and H. Lomax, 'Thin layer approximation and algebraic model for separated turbulent flows', *AIAA 16th Aerospace Sciences Meeting*, *AIAA paper*, 1978, pp. 78–257.
13. G.B. Deng and M. Visonneau, 'Evaluation of eddy-viscosity and second-moment turbulence closures for steady flows around ships', *Proc. of the 21st Symposium on Naval Hydrodymics*, Trondheim, Norway, June, 1996.
14. F. Sotiropoulos and V.C. Patel, 'Application of Reynolds-stress transport models to stern and wake flows', *J. Ship Res.*, **39**, 263 (1995).
15. Y. Sato, M. Sadatomi and K. Sekoguchi, 'Momentum and heat transfer in two-phase bubbly flow—I', *Int. J. Multiphase Flow*, **7**, 167 (1981).
16. M. Lance and J. Bataille, 'Turbulence in the liquid phase of a uniform bubbly air–water flow', *J. Fluid Mech.*, **22**, 95 (1991).
17. S.K. Wang, S.J. Lee, O.C. Jones and R.T. Lahey Jr., '3-D turbulence structure and phase distribution measurements in bubbly two-phase flow', *Int. J. Multiphase Flow*, **13**, 327 (1987).
18. D.A. Drew and R.T. Lahey Jr., 'The virtual mass and lift force on a sphere in rotating and straining inviscid flow', *Int. J. Multiphase Flow*, **13**, 113 (1987).
19. D.A. Drew and R.T. Lahey Jr., 'Some supplemental analysis on the virtual mass and lift force on a sphere in rotating and straining inviscid flow', *Int. J. Multiphase Flow*, **16**, 1127 (1990).
20. M. Ishii, 'Two-fluid model for two-phase flow', *Second International Workshop on Two-Phase Flow Fundamentals*, Rensselaer Polytechnic Institute, Troy, NY, 1987.
21. E. Loth, 'Model of two-phase turbulent dispersion in a planar free shear layer', To be presented at the *AIAA Aerospace Sciences Meeting*, January 1997.
22. R.W. Smith and M.C. Hyman, 'Convective-diffusive bubble transport in ship wakes', *NCSC TN*, 857-87, 1987.
23. F. Stern, E.G. Paterson and Y. Tahara, 'CFDSHIP-IOWA: Computational fluid dynamics method for surface-ship boundary layers and wake and wave fields', *Iowa Institute of Hydraulic Research Report 666*, Iowa City, Iowa, 1996.
24. J.F. Thompson, 'General curvilinear coordinate systems', *Appl. Math Comput.*, **10**, 1 (1982).
25. C.A.J. Fletcher, *Computational Techniques for Fluid Dynamics*, Springer, New York, 1988.

26. Y. Tahara, F. Stern and B. Rosen, ‘An interactive approach for calculating ship boundary layers and wakes for non-zero Froude number’, *J. Comput. Phys.*, **98**, 33 (1992).
27. S.V. Patankar, *Numerical Heat Transfer and Fluid Flow*, Hemisphere Publishing Corporation, NYC, 1980.
28. P.K Sweby, ‘High resolution TVD schemes using flux limiters’, in *Large-Scale Computations in Fluid Mechanics*, AMS, Providence, Rhode Island, 1985.
29. P. Roe, ‘Some contributions to the modelling of discontinuous flows’, in *Large-Scale Computations in Fluid Mechanics*, AMS, Providence, Rhode Island, 1985.
30. R.J. LeVeque and J.B. Goodman, ‘TVD schemes in one and two space dimensions’, in *Large-Scale Computations in Fluid Mechanics*, AMS, Providence, Rhode Island, 1985.
31. P. Tamamidis and D.N. Assanis, ‘Evaluation of various high-order accuracy schemes with and without flux limiters’, *Int. j. numer. methods fluids*, **16**, 931 (1993).
32. S.K. Saxena and K. Ravi, ‘Computation of three dimensional supersonic and hypersonic blunt body flows using high resolution TVD schemes based on Roe’s approximate Riemann solver’, *Lecture Notes in Physics*, **453**, 520 (1995).
33. W.K. Melville, E. Terrill and L. Ding, ‘Field measurements of air entrainment by breaking waves’, in *Air–Water Gas Transfer*, AEON Verlag & Studio, 63454 Hanau, 1996.
34. S.A. Thorpe, ‘On the clouds of bubbles formed by breaking wind waves in deep water, and their role in air–sea gas transfer’, *Phil. Trans. R. Soc. London Ser: A*, **304**, 155 (1982).